Neuron

Article

Different priming states of synaptic vesicles underlie distinct release probabilities at hippocampal excitatory synapses

Graphical abstract

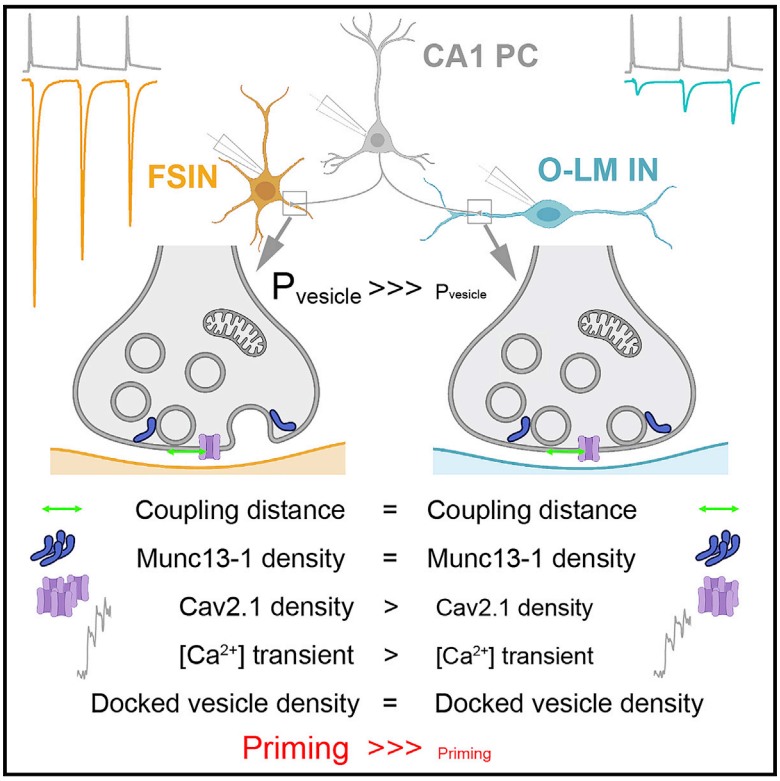

Authors

Mohammad Aldahabi, Flora Balint, Noemi Holderith, Andrea Lorincz, Maria Reva, Zoltan Nusser

Correspondence

nusser@koki.hu

In brief

Aldahabi et al. demonstrate that the target cell-type-dependent difference in release probability from hippocampal pyramidal cell axons is not the consequence of distinct coupling distances or nano-topologies of docked vesicles and Ca^{2+} channels. Instead, their data reveal robust differences in the priming state of docked vesicles.

Highlights

- Probability of release from pyramidal cells differs depending on the target cell type
- Replica immunolabeling reveals similar vesicle - Ca^{2+} channel coupling distances
- At low P_v synapses, PDBU is more effective in increasing P_v than elevating $[Ca^{2+}]$
- Similar docked vesicle densities suggest distinct priming states underlie different P_v

Aldahabi et al., 2022, Neuron *110*, 4144–4161
December 21, 2022
https://doi.org/10.1016/j.neuron.2022.09.035

CellPress

CellPress
OPEN ACCESS

Neuron

Article

Different priming states of synaptic vesicles underlie distinct release probabilities at hippocampal excitatory synapses

Mohammad Aldahabi,[1,2,5] Flora Balint,[1,5] Noemi Holderith,[1,5] Andrea Lorincz,[1,5] Maria Reva,[3,4] and Zoltan Nusser[1,6,*]
[1]Laboratory of Cellular Neurophysiology, Institute of Experimental Medicine, Budapest 1083, Hungary
[2]János Szentágothai School of Neurosciences, Semmelweis University, Budapest, Hungary
[3]Unit of Synapse and Circuit Dynamics, CNRS UMR 3571, Institute Pasteur, Paris, France
[4]Current address: Blue Brain Project, École Polytechnique Fédérale de Lausanne, Geneva, Switzerland
[5]These authors contributed equally to this work
[6]Lead contact
*Correspondence: nusser@koki.hu
https://doi.org/10.1016/j.neuron.2022.09.035

SUMMARY

A stunning example of synaptic diversity is the postsynaptic target cell-type-dependent difference in synaptic efficacy in cortical networks. Here, we show that CA1 pyramidal cell (PC) to fast spiking interneuron (FSIN) connections have 10-fold larger release probability (P_v) than those on oriens lacunosum-moleculare (O-LM) interneurons. Freeze-fracture immunolabeling revealed that different nano-topologies and coupling distances between Ca^{2+} channels and release sites (RSs) are not responsible for the distinct P_v. Although $[Ca^{2+}]$ transients are 40% larger in FSINs innervating boutons, when $[Ca^{2+}]$ entry is matched in the two bouton populations, EPSCs in O-LM cells are still 7-fold smaller. However, application of a phorbol ester analog resulted in a ~2.5-fold larger augmentation at PC – O-LM compared to PC – FSIN synapses, suggesting incomplete docking or priming of vesicles. Similar densities of docked vesicles rule out distinct RS occupancies and demonstrate that incompletely primed, but docked, vesicles limit the output of PC – O-LM synapses.

INTRODUCTION

The postsynaptic target-cell-type-dependent variation in vesicle release probability (P_v) and short-term plasticity is an intriguing feature of cortical networks. In the neocortex and hippocampus, when a pyramidal cell (PC) axon innervates a parvalbumin (PV)-expressing, fast-spiking interneuron (FSIN), it releases glutamate with a high P_v and the postsynaptic response shows short-term depression, whereas when the same axon establishes synapses onto a somatostatin (Som)/mGluR1α-expressing IN (e.g. oriens lacunosum-moleculare [O-LM] cells in the hippocampus), the P_v is low and the postsynaptic response displays robust short-term facilitation (Ali et al., 1998; Ali and Thomson, 1998; Reyes et al., 1998; Scanziani et al., 1998; Sun et al., 2005). These different presynaptic behaviors, together with distinct intrinsic properties of the postsynaptic INs, allow dynamic routing of activity within the neuronal network by shifting inhibition on the somato-dendritic domains of PCs in an activity-dependent manner (Pouille and Scanziani, 2004). As with many such important phenomena, identifying the mechanisms underlying the functional differences has been in the focus of research of the past two decades (Eltes et al., 2017; Koester and Johnston, 2005; Losonczy et al., 2003; Rozov et al., 2001; Stachniak et al., 2019; Sylwestrak and Ghosh, 2012).

Although the exact mechanisms are still elusive, many pieces of the puzzle have been put together. For example, pharmacological and molecular experiments revealed a role of constitutively active presynaptic mGluR7 receptors (Losonczy et al., 2003; Stachniak et al., 2019), which are preferentially located in PC active zones (AZs) that innervate Som INs (Shigemoto et al., 1996). Extracellular leucine rich repeat and fibronectin Type III domain containing 1 protein (Elfn1) is selectively expressed in Som INs and transsynaptically recruits and activates mGluR7 in a glutamate-independent manner (Stachniak et al., 2019; Tomioka et al., 2014), which in turn reduces P_v. At some PC – Som IN synapses, a role for presynaptic kainate receptors (GluK2) has been proposed in boosting short-term facilitation (Stachniak et al., 2019; Sylwestrak and Ghosh, 2012). However, when these presynaptic receptors were blocked or genetically removed, EPSCs at PC – Som IN synapses remained small and still displayed short-term facilitation, demonstrating the existence of additional key factors (Holderith et al., 2022). Examining the effects of fast and slow Ca^{2+} buffers on release, Rozov et al. (2001) concluded that a longer coupling distance between presynaptic voltage-gated Ca^{2+} channels (VGCCs) and the Ca^{2+} sensor on synaptic vesicles (SVs) might be responsible for the low P_v at PC – Som IN synapses in juvenile neocortex. The

easiest explanation of this result is that the presynaptic VGCC density is smaller at the low P_v synapses. A previous study from our laboratory tested this hypothesis and found only a 15% difference in VGCC density (Eltes et al., 2017). However, it became apparent that the coupling distance cannot be predicted from the density of VGCCs alone because docked SVs and VGCCs do not have random distributions within the AZs. Indeed, distinct non-random nanoscale topologies of SVs and VGCCs have been proposed at different synapses: e.g. rows of VGCCs are located along the SV (Dittrich et al., 2013; Luo et al., 2011; Neef et al., 2018), VGCCs are clustered next to the release sites (RSs) (perimeter release model; Nakamura et al., 2015; Rebola et al., 2019), or VGCCs are excluded from an area around the RSs (exclusion zone model [EZ]; Keller et al., 2015; Rebola et al., 2019).

A recent study (Rebola et al., 2019) provided compelling evidence for the unpredictability of synaptic strength from the magnitude of presynaptic Ca^{2+} influx and VGCC density. Cerebellar parallel fiber synapses have a low P_v and show paired-pulse facilitation, whereas molecular layer interneuron (MLIN) synapses have higher P_v and display short-term depression. Interestingly, action potential (AP)-evoked Ca^{2+} influx and VGCC density is much higher at the weak parallel fiber synapses. However, when the nanoscale arrangements of RSs and VGCCs were examined, a larger coupling distance was found in the weak synapse. At parallel fiber AZs, VGCCs are excluded from an ~50 nm area around the RSs, whereas in the strong IN synapses, much fewer VGCCs are clustered right next to the RSs (15–20 nm; Rebola et al., 2019). Because these results clearly demonstrate the necessity of knowing the nano-topologies of RSs and VGCCs to predict the strength of a synapse, here, we tested this for PC – FSIN and PC – O-LM cell synapses with high-resolution electron microscopy (EM) SDS-digested freeze-fracture replica immunolabelling (SDS-FRL) in the hippocampal CA1 area of adult mice.

An alternative explanation of the low P_v of PC – O-LM synapses is the low occupancy of the RSs by SVs. The P_v can be conceptualized as the function of a probability that an RS (or docking site as a synonym) is being occupied by an SV (P_{occ}) and a probability with which a docked vesicle is released (P_{succ} or P_{fusion}) upon the arrival of an AP ($P_v = P_{occ} * P_{fusion}$; Lin et al., 2022; Malagon et al., 2020; Neher, 2017; Quastel, 1997). Although it is challenging to peel out the contributions of these two factors, Malagon et al. (2020) analyzed the release at cerebellar parallel fiber – MLIN simple synapses and found that P_{occ} under physiological $[Ca^{2+}]_e$ (1.5 mM) is only 0.2, mainly accounting for the low P_v at these synapses. Thus, another possibility explaining the mechanisms underlying the low P_v at PC – O-LM synapses is a low P_{occ}, which we also test here with a combined *in vitro* physiological and pharmacological approach together with serial section EM and EM tomography.

RESULTS

Different amplitudes and short-term plasticity of unitary EPSCs in O-LM cells vs. FSINs

Dual whole-cell patch-clamp recordings were performed between CA1 PC – O-LM cells and PC – FSINs in acute brain slices obtained from adult transgenic mice in which O-LM cells express the red fluorescent protein tdTomato (see STAR Methods). We have *post hoc* verified the morphological identity of 45 red cells with somatic locations in the stratum oriens, out of which 43 INs had O-LM morphology and only two were bistratified cells, demonstrating that >95% of the red cells belong to a well-defined IN subtype. We selected FSINs based on the lack of red fluorescence and on the size, shape, and location of their somata as visualized with DIC imaging. Their fast-spiking behavior was tested with somatically injected DC currents of variable amplitudes at the beginning of the whole-cell recording period (Karlocai et al., 2021). Single PC action potentials (APs) often failed to evoke unitary EPSCs (uEPSCs) in O-LM cells (failure rate: 82 ± 12%) in 2 mM external $[Ca^{2+}]_e$, and, as a consequence, the mean uEPSC amplitude was only 9.4 ± 9.5 pA (Figures 1A, 1C, 1D, and 1F; n = 96 pairs). A short train of APs at 40 Hz evoked uEPSCs with robust short-term facilitation (paired pulse ratio [PPR]: 2.26 ± 1.07, n = 79 pairs; Figures 1A and 1D–G) consistent with previous data recorded in juvenile rats and mice. In contrast, uEPSCs had large amplitudes in FSINs (142.9 ± 145.9, n = 70; Figures 1B, 1D, and 1F) and showed on average paired-pulse depression (PPR: 0.92 ± 0.31, n = 70; Figures 1D, 1E, and 1G). A previous study from our laboratory (Karlocai et al., 2021) demonstrated that the P_v of PC – FSIN synapses in 2 mM $[Ca^{2+}]_e$ is 0.42, and it is 0.04 ± 0.04 in PC – O-LM cell synapses (M.A., N.H., and Z.N., unpublished data), indicating that the main reason for the 15-fold difference in the uEPSC amplitude is primarily the consequence of a robust, ~10-fold difference in the initial P_v of the synapses.

Freeze-fracture replica labeling reveals similar distribution of Munc13-1 and Cav2.1 in PC AZs contacting O-LM cells and FSINs

To test whether different nano-topologies of RSs and VGCCs (Rebola et al., 2019) underlie the distinct initial P_v of PC – FSIN vs. PC – O-LM cell synapses, we performed EM SDS-FRL of Munc13-1, as a molecular marker of the RS (Reddy-Alla et al., 2017; Sakamoto et al., 2018), and Cav2.1, a key VGCC subunit, at excitatory hippocampal/cortical synapses (Holderith et al., 2012; Rozov et al., 2001). Because Cav2.2, the other dominant VGCC subunit, cannot be localized with similar efficiency, we decided to concentrate on the Cav2.1 subunit but first probed the postsynaptic responses under conditions when release is mainly mediated by this subunit. We performed paired recordings between CA1 PCs and FSINs in 1 μM ω-conotoxin GVIA, a selective N-type (Cav2.2) VGCC blocker, and found that a target cell-type-specific close proximity of the Cav2.2 subunit to the SVs cannot explain the high P_v of the PC – FSIN synapses (Figures 1H–1J). Namely, although 1 μM ω-conotoxin reduced the amplitude of the first uEPSC of the train by 20% (BSA control: 126.7 ± 101.4 pA, n = 17; ω-conotoxin: 103.7 ± 120.7 pA, n = 18 pairs), without a clear change in the PPR (control: 0.92 ± 0.31; BSA control: 1.00 ± 0.34; ω-conotoxin: 1.02 ± 0.37), the amplitude of uEPSCs in FSINs still remained ~18-fold larger than that recorded in O-LM cells in ω-conotoxin (5.7 ± 0.4 pA, n = 5), demonstrating that these two synapse populations function vastly differently even if the release is mediated mainly by P/Q-type (Cav2.1) VGCCs.

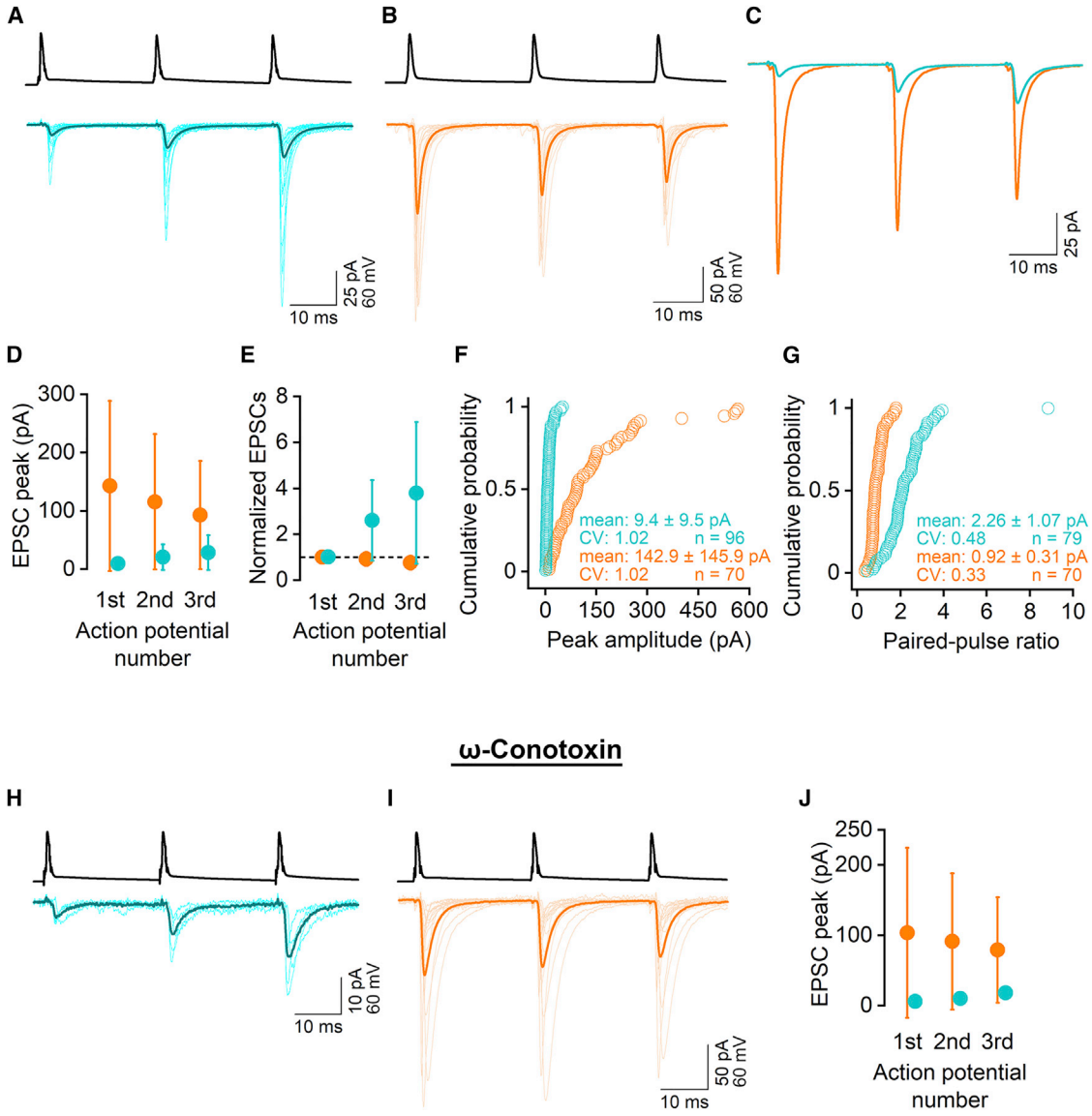

Figure 1. Distinct EPSC amplitudes and short-term plasticity of CA1 PC – FSINs vs. PC – O-LM cell synapses

(A and B) Averaged postsynaptic responses evoked by three action potentials (at 40 Hz) in presynaptic PCs are shown in O-LM cells (A, thin traces: 17 individual pairs; thick trace: the average of 96 pairs) and FSINs (B, thin traces: 16 individual pairs, thick trace: the average of 70 pairs). The amplitude of the first uEPSCs and the short-term plasticity of the responses show large variability within groups but are considerably different between O-LM cells and FSINs.

(C) Superimposed PC – O-LM (cyan, average of 96 pairs) and PC – FSIN (orange, average of 70 pairs) uEPSCs demonstrate the dramatic difference in the amplitude (the first EPSC is ~15 times larger in FSINs) and short-term plasticity.

(D) The amplitudes (mean ± SD) of the uEPSCs in O-LM (n = 96 pairs) and FSINs (n = 70 pairs) are shown for the three consecutive APs.

(E) Same as in (D), but normalized amplitude values are shown for demonstration of the difference in the short-term plasticity of the responses.

(F and G) Cumulative probability plots of the peak amplitude of the first uEPSC (F) and the paired-pulse ratio (G) in O-LM cells (cyan) and FSINs (orange). Mean ± SD, coefficient of variations (CV), and number of pairs are shown in the figure. For 17 PC – O-LM pairs, first uEPSC was 0 pA, precluding the calculation of PPR (G).

(H) Same as (A) but in the presence of 1 μM ω-conotoxin to block N-type Ca^{2+} channels (thin traces: 5 individual pairs; thick trace: the average of 5 PC – O-LM pairs).

(I) Same as (B) but in the presence of 1 μM ω-conotoxin (thin traces: 16 individual pairs; thick trace: the average of 18 PC – FSIN pairs).

(J) Same as (D) but in the presence of 1 μM ω-conotoxin (n = 5 PC – O-LM pairs and n = 18 PC – FSIN pairs, mean ± SD).

To compare sub-AZ distribution of Munc13.1 and Cav2.1 in these two synapse populations using SDS-FRL, the postsynaptic targets need to be identified. FSINs express Kv3.1b, a voltage-gated K^+-channels subunit, and the majority of O-LM cells express mGluR1α (Eltes et al., 2017). We used the mirror replica method, in which corresponding extracellular (E-face, EF) and protoplasmic (P-face, PF) plasma membrane faces of the same structure can be identified and

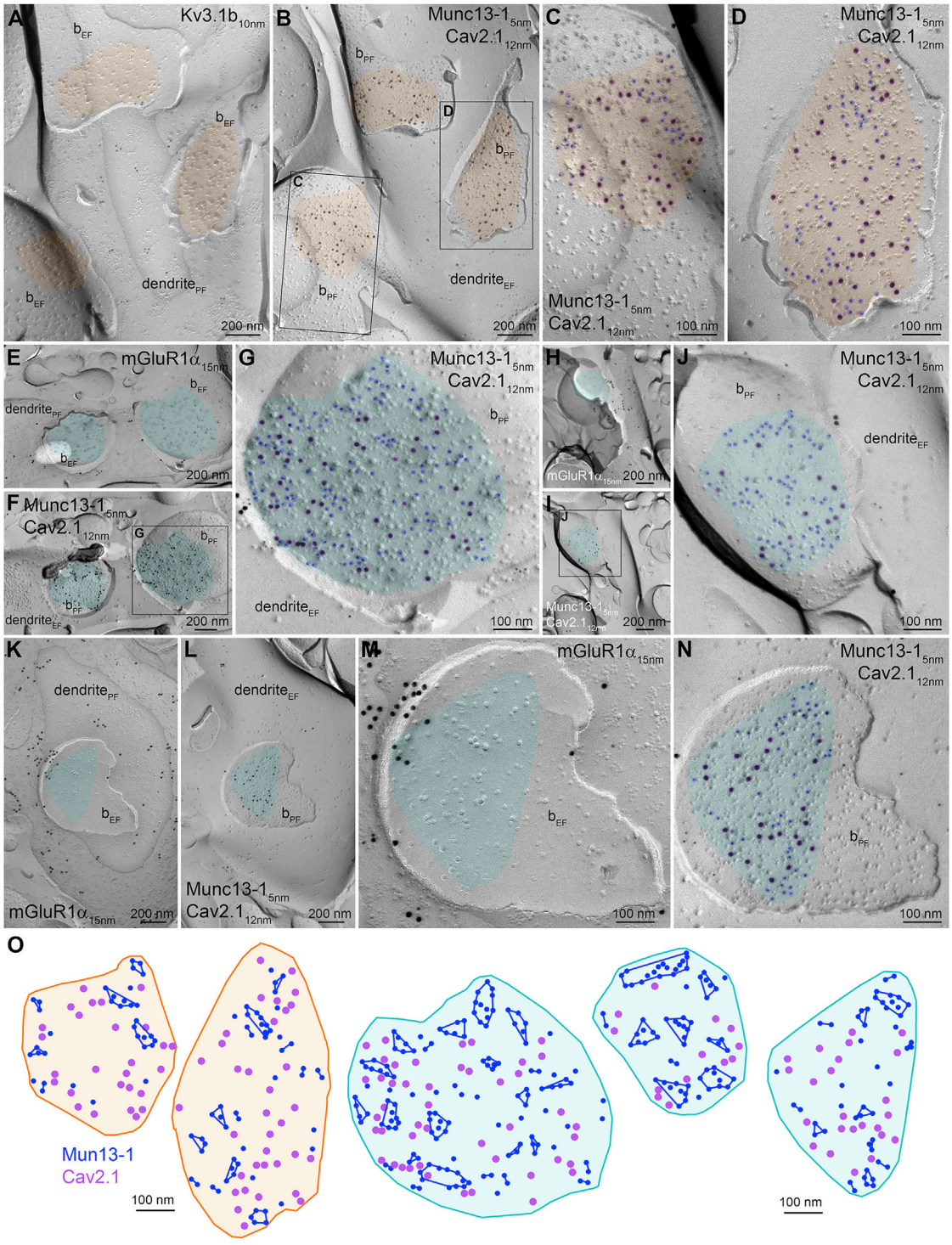

Figure 2. Freeze-fracture replica immunolabeling of Munc13-1 and Cav2.1 in excitatory synapses on Kv3.1b+ and mGluR1α+ INs

(A) Low magnification image of the protoplasmic membrane face (PF) of a Kv3.1b+ dendrite ($dendrite_{PF}$) targeted by three excitatory boutons (b_{EF}) with fully exposed AZs (highlighted in orange).

(B) The mirror replica of that shown in (A) immunolabeled for Munc13.1 and Cav2.1. Gold particles are concentrated in the AZs (orange) on the PF membrane of the boutons (b_{PF}).

(C and D) High magnification images of the boxed areas in (B) showing a small (C) and a large (D) AZ. Gold particles are highlighted in blue (Munc13-1) and purple (Cav2.1).

(legend continued on next page)

labeled in matching replica pairs (Figure 2). Gold particles labeling Munc13-1 and Cav2.1 proteins were accumulated in the AZs of axon terminals fractured onto somato-dendritic membranes of INs identified on the matching replicas by gold particles labeling Kv3.1b (Figures 2A–2D) or mGluR1α (Figures 2E–2O).

First, we compared the density and sub-AZ distribution of Munc13-1 in these two synapse populations. The enrichment of intramembrane particles in AZs in the PF plasma membrane allowed the demarcation of the AZs (see STAR Methods and Figure S1) and revealed that the AZs on mGluR1α positive INs (0.10 ± 0.048 μm^2, n = 118) are 43% larger than those on Kv3.1b positive structures (0.07 ± 0.035 μm^2, n = 159; Figure 3A) with similar Munc13-1 densities (Figure 3B). Next, we asked whether the distribution of Munc13-1 particles is significantly different from random distributions. We generated 200 random distributions of gold particles in each AZ, measured the mean nearest neighbor distances (NNDs) between the particles, and compared them to the NNDs of the data. Our results revealed that the NNDs were significantly shorter compared to those of the randomly placed particles in both synapse populations (Figure 3C), indicating potential clustering of the particles. To directly test this, we performed Ripley's analysis at individual AZs, an approach that is particularly sensitive to particle clustering (Rebola et al., 2019). In 66% and 81% of the AZs contacting Kv3.1b- and mGluR1α-positive dendrites, respectively, the distributions of gold particles were significantly different from random (Figure 3D). DBSCAN clustering then revealed an average of 5.4 ± 2.5 (n = 105 AZs) and 7.9 ± 4.3 (n = 96 AZs) clusters per AZ on Kv3.1b- and mGluR1α-positive structures, respectively (Figure 3E). This difference in the cluster number is fully explained by the AZ size difference, as demonstrated by the similar Munc13-1 cluster densities in these AZ populations (Figure 3F). Even the within-AZ distributions of the Munc13-1 clusters are similar in these synapses, as the cluster to cluster mean NNDs show no significant difference (Figure 3G). We then analyzed the number of gold particles labeling Munc13-1 per cluster in both synapse populations (Kv3.1b: mean = 4.5 ± 3 gold/cluster, CV = 0.67, n = 571 clusters; mGluR1α: mean = 4.7 ± 3.6 gold/cluster, CV = 0.76, n = 754 clusters), and found no significant difference between them (p = 0.479, Mann-Whitney U-test [MWU test]).

Next, we examined the distribution and density of Cav2.1 subunit with SDS-FRL and found a small but significant difference in the density of Cav2.1 in these synapses (normalized density: mGluR1α: 1.0 ± 0.3, n = 69 AZs, Kv3.1b: 1.2 ± 0.46, n = 123; Figure 3H), consistent with our previous study performed in the CA3 area of juvenile rats (Eltes et al., 2017). The mean NNDs of randomly placed particles were significantly different from those of the data (Figure 3I). However, Ripley's H function analysis revealed that in the majority of AZs (Kv3.1b: 92%, mGluR1α: 84%) the distributions were not compatible with clustering (Figure 3J), indicating a non-random, but not clustered, distribution. Such a distribution of Cav2.1 subunit is similar to that found in cerebellar parallel fiber synapses (Rebola et al., 2019). The clustering of Munc13-1 and the lack of clustering of Cav2.1 (Figure 2O) suggest that the Ca^{2+} channels might be excluded from an area around the vesicles (EZ). To test this, we performed the bivariate version of Ripley's analysis in those synapses in which the Munc13-1 molecules showed clustered distributions and found that $H_{biv(r)}$ values were significantly different from random in 95% and 100% of AZs synapsing onto Kv3.1b- and mGluR1α-positive structures, respectively ($p < 0.05$, MAD test). Population level comparisons of normalized $H_{biv(r)}$ values (Figures 3K and 3L) demonstrate a repellent interaction between these particles ($p < 0.00003$, MAD test). The distance between the Munc13-1 clusters and the nearest Cav2.1 gold particles was significantly shorter than those between the Munc13-1 clusters in both synapse populations (Figure 3M).

Because our data are consistent with an EZ model, next we aimed to determine the EZ radius, the size of the area from which the Ca^{2+} channels are excluded around the vesicles. In each AZ, we determined the center of gravity of each Munc13-1 cluster and created circular EZ areas around them with radii ranging from 30 to 60 nm. Gold particles were randomly placed within the AZs but outside the EZ areas and the mean NNDs were measured and compared to those of the data (Figure 4). Statistical comparisons revealed that EZ radii of 40 and 50 nm resulted in mean NNDs that were not significantly different from the data, and it was the same in both synapse populations (Figures 4B and 4D).

Smaller Ca^{2+} influx is not the main reason for the low P_v at PC – O-LM cell synapses

Having excluded that different nano-topologies and coupling distances are the fundamental differences between these two synapse populations, and having confirmed our previous results (Eltes et al., 2017) showing a significantly larger Cav2.1 subunit density in FSIN innervating AZs, next we addressed the issue of whether the low P_v at PC – O-LM cell synapses is the consequence of lower Ca^{2+} influx. We have conducted two-photon [Ca^{2+}] imaging experiments in local axon collaterals of CA1 PCs in acute *in vitro* slices using intracellularly applied Fluo5F (Figure 5). Following the imaging, the slices were fixed, biocytin was visualized, and the slices were immunoreacted for PV and mGluR1α to visualize FSINs and O-LM cells, respectively (Figures 5I–5K; see Eltes et al., 2017). First, we monitored the change in [Ca^{2+}] transients within the course of our ~30 min imaging period and found that in the presence of normal artificial cerebrospinal fluid (ACSF) the amplitudes remain stable (from 0.17 ± 0.08 G/G_{max} to 0.15 ± 0.06 G/G_{max}, n = 11 cells; Figures 5C and 5G). When the amplitudes of [Ca^{2+}] transients in boutons contacting PV and mGluR1α immunopositive structures were examined, a 38% larger amplitude in the PV-positive

(E–N) Low (E, F, H, I, K, L) and high (G, J, M, N) magnification replica images immunolabeled for mGluR1α, Munc13-1, and Cav2.1. (E) and (F), (H) and (I), (K) and (L), and (M) and (N) are mirror replica images of the same dendrites. AZ areas are shown in cyan; gold particles are highlighted in blue (Munc13-1) and purple (Cav2.1). (O) Delineated AZs on Kv3.1b+ (orange) and mGluR1α+ (cyan) dendrites (original images shown in C, D, G, J, and N) showing gold particles labeling Cav2.1 (purple) in relation to Munc13-1 clusters (blue). Clustering was performed with DBSCAN.

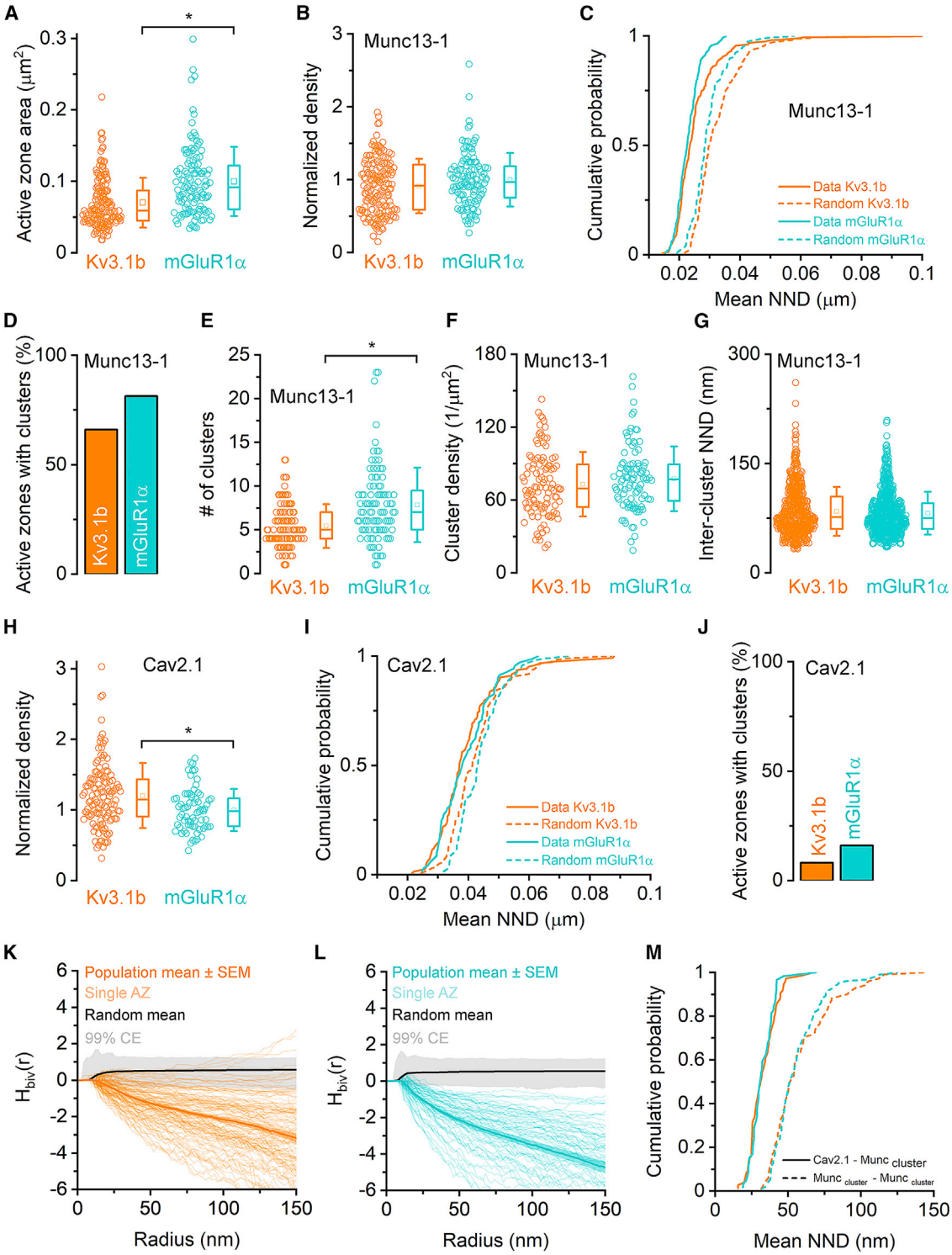

Figure 3. Quantitative analysis of Munc13-1 and Cav2.1 immunolabeling in AZs synapsing on Kv3.1b+ and mGluR1α+ INs

(A) The AZs are significantly ($p = 7 \times 10^{-9}$, MWU test) larger on mGluR1α+ INs (0.10 ± 0.048 μm², n = 118) than on Kv3.1b+ cells (0.07 ± 0.035 μm², n = 159).

(B) The normalized density of Munc13-1 immunolabeling is similar (p = 0.081, MWU test) in both synapse populations.

(C) Cumulative probability plots of the mean nearest neighbor distances (NNDs) of gold particles (data, solid lines) and those of randomly placed particles (dotted lines). The mean NNDs of the data are significantly ($p < 0.001$, Kruskal-Wallis [KW] test followed by Wilcoxon signed-rank [WSR] test with Holm-Bonferroni

(legend continued on next page)

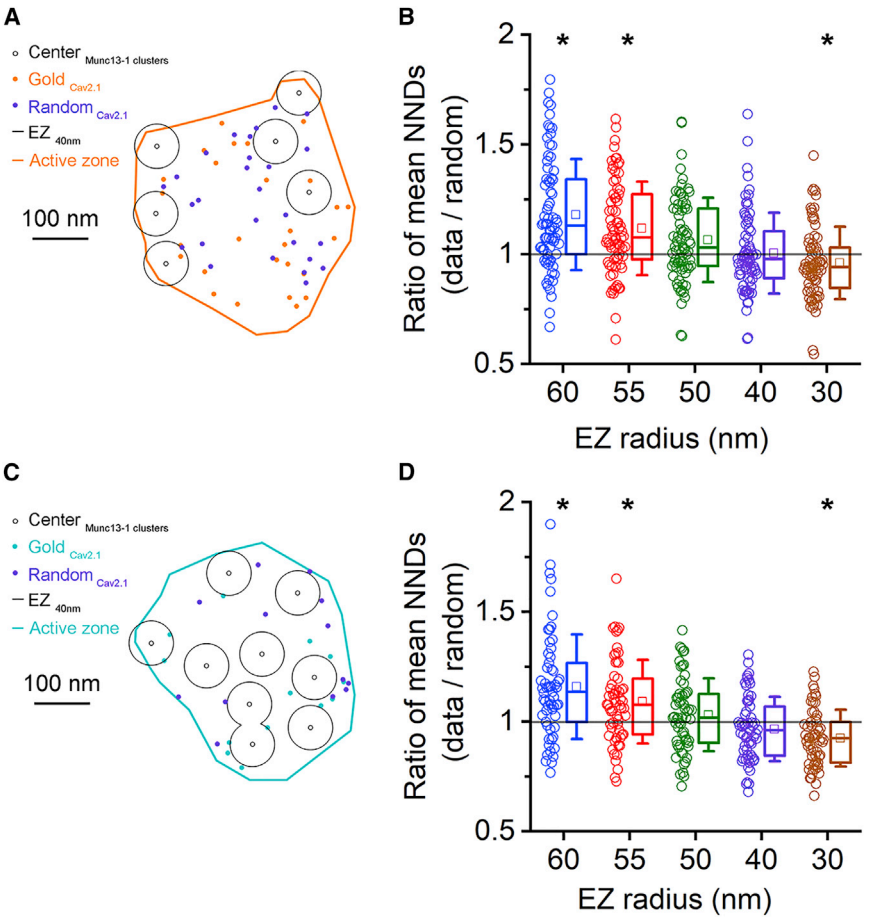

Figure 4. An exclusion zone model reveals similar nanoscale distribution of Cav2.1 in AZs on Kv3.1b+ and mGluR1α+ INs

(A) An AZ on a Kv3.1b+ dendrite is shown (demarcated with orange line). Centers of experimentally determined Munc13-1 clusters (small black open circles) are surrounded by exclusion zones of 40 nm radius (EZ $_{40nm}$, large circles), the original positions of the Cav2.1 gold particles are shown with orange dots, and the locations of the same number of randomly placed particles generated by the exclusion zone model (EZM) are shown by the purple dots.

(B) Ratios of mean NNDs calculated from experimental and an EZM-generated Cav2.1 pattern are plotted for 5 different exclusion zone radii (n = 74 AZs, 50 random simulations per AZ). Corresponding data (open circles) and their boxplot summary are colored identically. Random patterns at 60, 55, and 30 nm EZ radii are significantly different from the data ($p < 0.01$, Friedman test followed by WSR test with HBC).

(C) Same as (A) but for an AZ contacting an mGluR1a+ dendrite.

(D) Same as (B) but showing ratios of mean NNDs from AZs contacting mGluR1a+ dendrites (n = 59 AZs). Random patterns at 60, 55, and 30 nm EZ radii are significantly different form the data ($p < 0.003$, Friedman test followed by WSR test with HBC). Horizontal lines in the box plots: 25th, 50th, and 75th percentiles, rectangle: mean, whiskers: SD.

dendrite-targeting boutons was found (mGluR1α: 0.16 ± 0.06 G/G_{max}, n = 25 boutons; PV: 0.22 ± 0.08 G/G_{max}, n = 16 boutons; Figures 5L and 5M), confirming our previous data obtained in CA3 PCs of juvenile rats (Eltes et al., 2017). We then aimed to increase the $[Ca^{2+}]$ transients in PC boutons innervating O-LM INs to match those recorded in PV-positive dendrite innervating axon terminals. We found that the K^+ channel blocker 4-AP at 5 μM increased $[Ca^{2+}]$ transients by 46% ± 29% in all imaged

correction [HBC]) smaller than those of randomly distributed gold particles within both AZ populations. The experimental NNDs are slightly longer in AZs on Kv3.1b+ cells (26 ± 10 nm) compared to those (23 ± 4 nm) on mGluR1α+ cells ($p = 0.02542$, KW test followed by MWU test with HBC).

(D) Ripley analysis of individual synapses demonstrates that Munc13-1 gold particles are clustered ($p < 0.05$, maximum absolute deviation [MAD] test) in 66% and 81% of the AZs on Kv3.1b+ (n = 159) and mGluR1α+ (n = 118) dendrites, respectively.

(E) The number of Munc13-1 clusters is significantly ($p = 0.000004$, MWU test) larger in mGluR1α+ (7.9 ± 4.3, n = 96) than in Kv3.1b+ (5.4 ± 2.5, n = 105) dendrites contacting AZs.

(F) The Munc13-1 cluster density does not differ in the two AZ populations ($p = 0.24$, MWU test).

(G) The center-to-center NND between Munc13-1 clusters is similar in the two AZ populations ($p = 0.43$, MWU test).

(H) The density of gold particles labeling Cav2.1 is significantly ($p = 0.0016$, MWU test) larger in AZs contacting Kv3.1b+ dendrites.

(I) Cumulative probability plots of the mean NNDs of gold particles labeling Cav2.1 (data, solid lines) and those of randomly placed particles (dashed lines). The mean NNDs of the data are significantly ($p < 0.001$, WSR test with HBC) different from randomly distributed gold particles within the same AZ population, but they are comparable between the two AZ populations ($p = 0.695$, MWU test with HBC).

(J) In only a small fraction of the AZs (Kv3.1b+: 8%, n = 123; mGluR1α+: 16%, n = 69), gold particles for Cav2.1 are clustered ($p < 0.05$, MAD test), as revealed by Ripley's analysis of individual AZs.

(K and L) Bivariate Ripley's analysis of the Cav2.1 and Munc13-1 gold particles in double labeling experiments in AZs contacting Kv3.1b+ (K) and mGluR1α+ (L) dendrites reveals a repellent interaction between the two types of molecules. Normalized $H_{biv}(r)$ is plotted for individual AZs (thin lines), and the population average is shown with the thick line. The thick black line is the mean $H_{biv}(r)$ of 500 random distributions generated for each AZ. Gray area is the 99% confidence envelope (CE).

(M) The mean NNDs between Cav2.1 gold particles and the edges of Munc13-1 clusters are significantly shorter ($p < 0.0001$ for both synapse populations, MWU test with HBC) than those between the Munc13-1 clusters in both synapse populations (orange: Kv3.1b+, cyan: mGluR1α+).

Horizontal lines in the boxplots: 25th, 50th, and 75th percentiles, rectangle: mean, whiskers: SD.

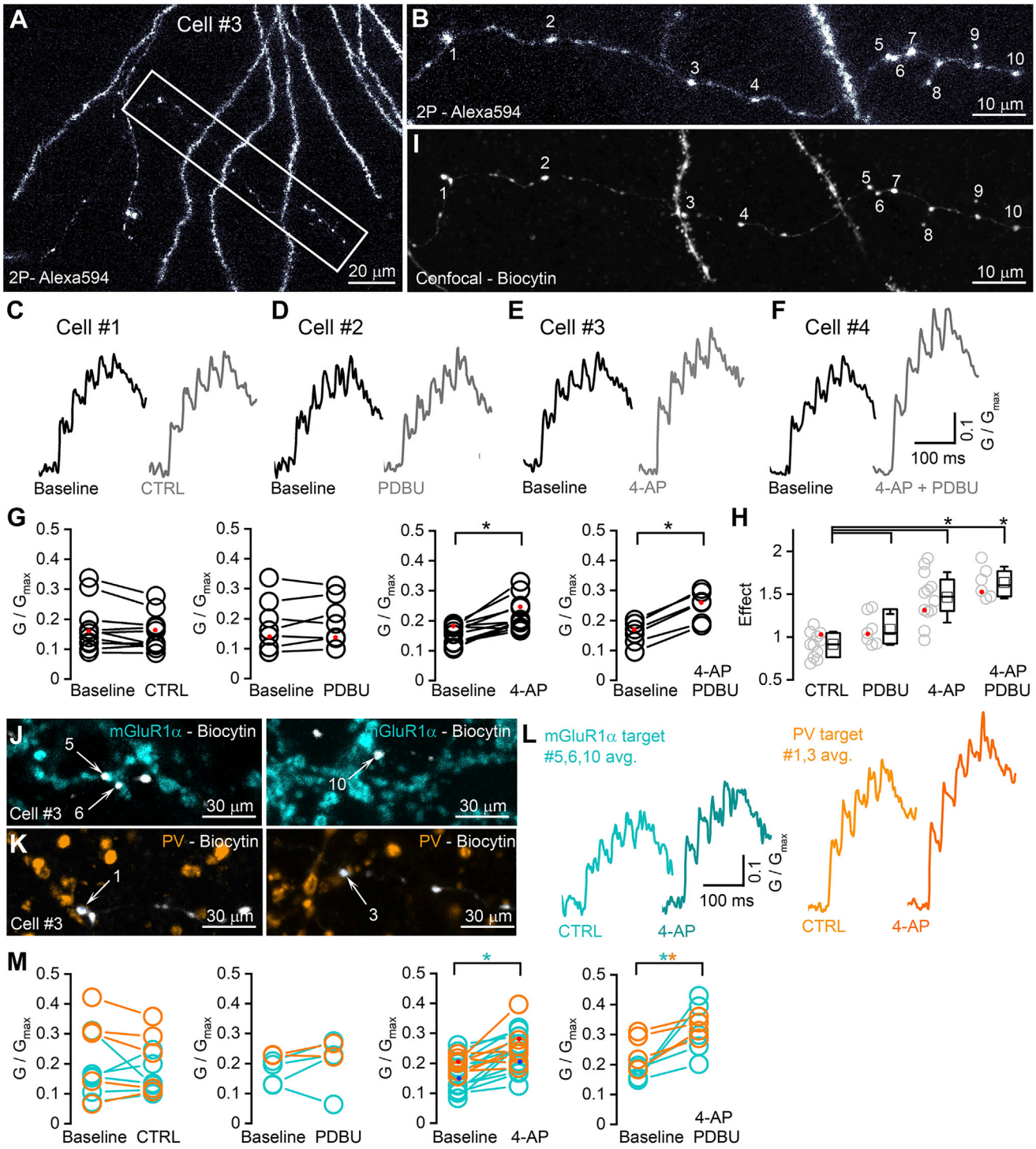

Figure 5. Effects of PDBU and 4-AP on the amplitudes of [Ca^{2+}] transients recorded from CA1 PC boutons targeting PV+ or mGluR1α+ INs

(A) Two-photon (2P) image stack of a CA1 PC (Cell #3) basal dendritic tree and axonal arbor filled with 20 µM Alexa Fluor 594 (white), 200 µM Fluo5F, and biocytin. Boxed area indicates the part of the imaged axonal arbor and is shown at higher magnification in (B).

(B) High magnification 2P image of the scanned axon collateral. Numbers indicate scanned boutons.

(C) Averaged [Ca^{2+}] transients evoked by 5 APs at 40 Hz in local axon collaterals of a CA1 PC (Cell #1, trace is average of 17 boutons, black). Each bouton was scanned at the beginning of the imaging period (Baseline, black) and 30 min later (CTRL, gray) without perfusing any drug.

(D–F) Same as (C) for Cells #2–4 but, after a control imaging period (Baseline), 1 µM PDBU (D), 5 µM 4-AP (E), or both (F) were applied (average trace from 9, 12, and 21 boutons, respectively).

(legend continued on next page)

boutons (from 0.15 ± 0.03 G/G_{max} to 0.22 ± 0.05 G/G_{max}, n = 12 cells; Figures 5E and 5G), which was very similar when calculated from those boutons that contact mGluR1α-positive dendrites (from 0.16 ± 0.06 G/G_{max} to 0.24 ± 0.06 G/G_{max}, n = 12 boutons; Figure 5L and 5M). Thus, the presynaptic Ca^{2+} influx into mGluR1α-positive IN innervating boutons in 5 μM 4-AP (0.24 G/G_{max}) is even slightly larger than that recorded in PV-positive dendrite innervating axon terminals under control conditions (0.22 ± 0.08 G/G_{max}, n = 16 boutons). To test how the postsynaptic EPSC amplitudes are affected by this pharmacological manipulation, we performed paired whole-cell recordings between CA1 PCs – FSINs and PCs – O-LM cells in acute coronal hippocampal slices from adult mice (Figures 6 and 7). A previous study from our laboratory demonstrated that whole-cell recordings could cause robust rundown of the postsynaptic EPSCs when glutamate is not added into the intracellular solution of the presynaptic cell (Biro et al., 2005). Thus, we included 10 mM glutamate into the intracellular solution of the presynaptic PCs and conducted 30 min whole-cell recordings in control ACSF to test the stability of the postsynaptic responses. When the postsynaptic cell was a FSIN, the relative amplitude of the uEPSCs in the last 10 min of the recordings compared to the first 10 min was 0.99 ± 0.39 (n = 15 pairs; Figures 6A and 6B). However, to our surprise, when the postsynaptic IN was an O-LM cell, the same protocol resulted in a 48% rundown of the uEPSCs (normalized amplitude: 0.52 ± 0.51, n = 28 pairs; Figure S2A). The normalized EPSC amplitude change correlated tightly with the change in the success rate (Figure S2B), indicating that the rundown was the consequence of a postsynaptic cell-type-selective presynaptic dialysis of an unknown factor. To further verify this, we carried out a few paired recordings in which the presynaptic PC was recorded in the perforated patch configuration using gramicidin. Here, the relative EPSC amplitude at the end of the recordings was 0.94 ± 0.25 (n = 6), which was not significantly different from that recorded in the first 10 min (Figure S2C and S2D). The extremely low yield of finding connected pairs and keeping them stable without membrane rupture (that was monitored with a fluorescent dye in the pipette, see STAR Methods) prompted us to perform most of the pharmacological experiments in the dual whole-cell mode and *post hoc* correct the drug effects to the average rundown observed during the same time in ACSF.

5 μM 4-AP increased the amplitude of the first uEPSC of a short train at PC – O-LM connections by 166% ± 105% (from 11.0 ± 13.0 pA, median 5.2 pA to 21.6 ± 16.6 pA, median 16.8 pA, both rundown corrected, n = 11 pairs; Figures 7B and 7E), but the amplitude of the uEPSCs is still ∼7-fold smaller compared to PC – FSIN connections (21.6 ± 16.6 pA vs. 142.9 ± 145.9 pA), demonstrating that the difference in $[Ca^{2+}]$ transients is not the main reason for the different P_v and for arguing against P_{fusion} as the main factor underlying the low P_v at PC – O-LM cell synapses.

When effects of 5 μM 4-AP on uEPSC amplitudes in O-LM and FSINs were compared, a smaller increase was found at PC – FSIN connections (50% ± 59% increase from 139.2 ± 150.7 pA to 175.1 ± 141.7 pA, n = 12 pairs; Figure 6C), indicating a somewhat smaller initial P_{fusion} of PC – O-LM cell compared to that at PC – FSIN synapses (Figure 7E).

Differential effects of PDBU indicate distinct docking or priming at PC – FSIN vs. PC – O-LM cell synapses

Next, we aimed to selectively manipulate the P_{occ} at these synapses by applying the phorbol ester analog phorbol 12,13-dibutyrate (PDBU; 1 μM). Consistent with the high P_v of PC – FSIN synapses, PDBU increased the first uEPSC amplitude of the train by only 77% ± 115% (Figure 6D) and reduced the PPR from 0.97 ± 0.40 to 0.72 ± 0.37 (n = 8). In contrast, PDBU resulted in a much larger increase (4.4 ± 3.1-fold) at PC – O-LM cell synapses (from 11.4 ± 7.5 pA to 43.9 ± 40.2 pA, n = 9; Figures 7C and 7E, data from perforated patch-clamp recordings). This 4.4-fold increase by PDBU and the 2.5-fold increase by 4-AP altogether indicate a ∼11-fold increase in uEPSC amplitude in O-LM cells when both drugs are applied together. We performed these experiments and indeed found a 11.9 ± 12.2-fold (n = 12; Figures 7D and 7E, whole-cell recording and rundown corrected), but widely variable (from no change to a 46-fold increase, coefficient of variation: CV = 1), degree of increase at PC – O-LM cell synapses. In contrast, only a 1.7 ± 0.6-fold increase with smaller variability (CV = 0.36) was detected at PC – FSIN synapses (Figures 6E and 7E). Although the reason for the large variability in the drug effect is unknown, the large variability in the degree of rundown (CV = 0.98; from total rundown to no rundown) could have a key contribution to it. It is important to note that the effects of 5 μM 4-AP and 1 μM PDBU were additive

(G) Peak amplitudes of $[Ca^{2+}]$ transients for the first AP do not change in CTRL and in PDBU but increase significantly following the application of 4-AP and 4-AP + PDBU (WSR test, p = 0.10, 0.35, 0.003, 0.036, respectively). Data points represent individual cells (CTRL: n = 11; PDBU: n = 7; 4-AP: n = 12; 4-AP + PDBU: n = 6). Red dots indicate the cells shown in (C–F).

(H) KW test with post hoc Dunn's test demonstrates that 4-AP (p = 0.0009) and 4-AP + PDBU (p = 0.0003) have significant effects on the peak amplitudes of $[Ca^{2+}]$ transients compared to control, while PDBU does not change the transients significantly (p = 1). Data points represent individual cells (CTRL: n = 11; PDBU: n = 7; 4-AP: n = 12; 4-AP + PDBU: n = 6). Red dots indicate the cells shown in (C–F).

(I) Maximum intensity projection of a confocal image z stack showing the imaged boutons after fixation and the visualization of biocytin. Each imaged bouton can be unequivocally identified.

(J and K) Some of the imaged boutons are in direct contact with mGluR1α+ (J, #5, 6, 10) or PV+ (K, #1, 3) dendrites.

(L) Averaged $[Ca^{2+}]$ transients evoked by 5 APs at 40 Hz in boutons #5, 6, and 10 targeting mGluR1α+ (cyan CTRL, dark cyan 4-AP) and in boutons #1 and 3 targeting PV+ dendrites (CTRL, light orange, 4-AP, dark orange). $[Ca^{2+}]$ transients are smaller in boutons targeting mGluR1α+ dendrites.

(M) Peak amplitudes of averaged $[Ca^{2+}]$ transients in response to the first AP in boutons with identified postsynaptic partners (cyan mGluR1α+, orange PV+) in CTRL and in the presence of drugs (CTRL: p = 0.87 and 0.50, n = 6 and 5 cells; PDBU: p = 0.42, n = 4 cells only for mGluR1α+; 4-AP: p = 0.0012 and 0.06, n = 12 and 11 cells; 4-AP + PDBU: p = 0.031 and 0.032, n = 5 and 4 cells for mGluR1α+ and PV+ INs, respectively, paired t test). Red and blue dots indicate data from Cell #3.

Horizontal lines in the boxplots: 25th, 50th, and 75th percentiles, rectangle: mean, whiskers: SD.

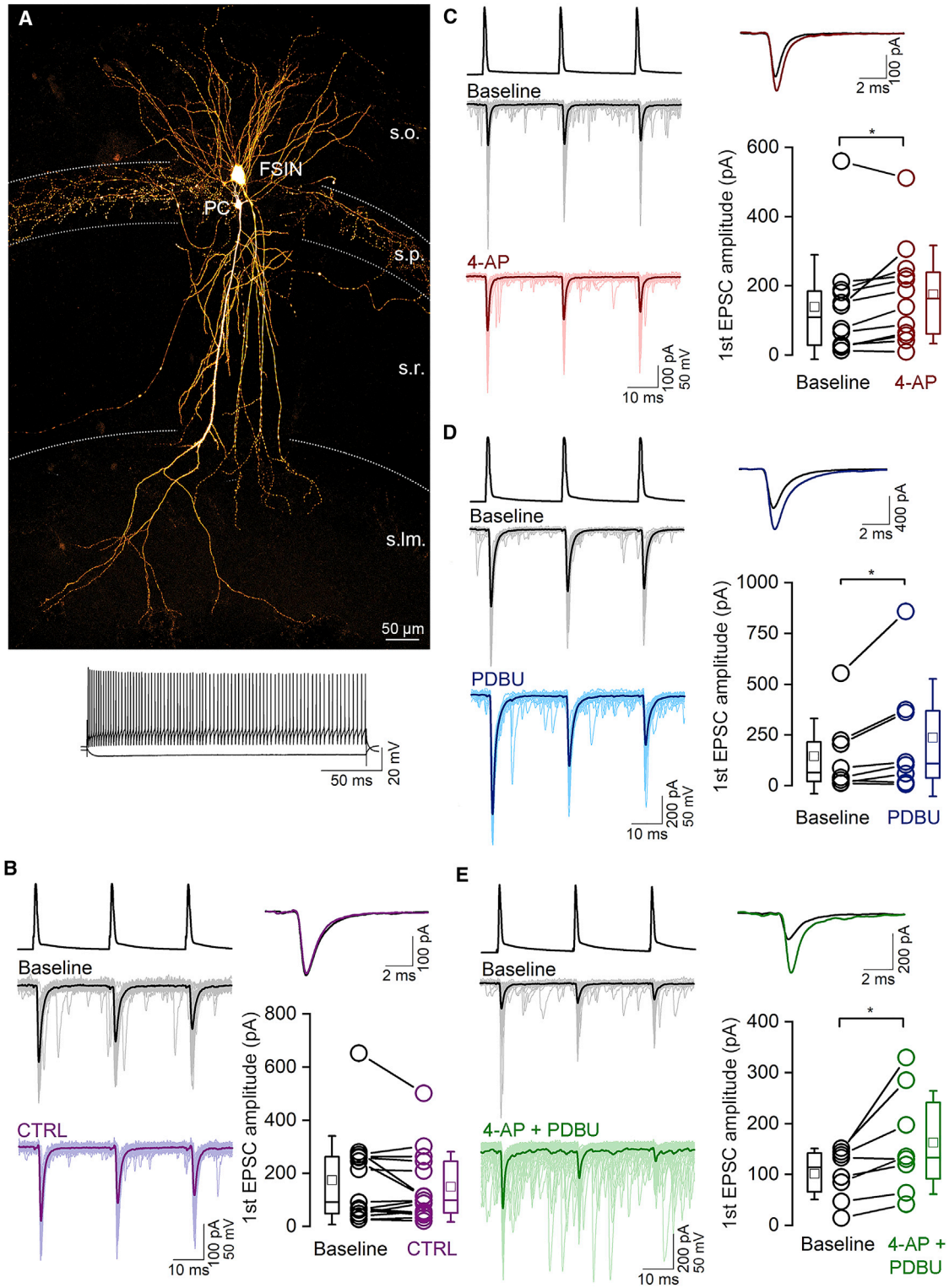

Figure 6. Synaptic responses between CA1 PCs and FSINs have moderate sensitivity to PDBU and 4-AP

(A) Confocal maximum intensity projection image of a biocytin-filled, synaptically connected PC – FSIN pair in the hippocampal CA1 region (top). Membrane potential responses of the IN to depolarizing and hyperpolarizing current pulses are shown demonstrating the FS firing characteristic of the cell (bottom). s.o., stratum oriens; s.p., stratum pyramidale; s.r., stratum radiatum; s.lm., stratum lacunosum-moleculare.

(legend continued on next page)

in PC – O-LM cell synapses, consistent with different sites of action and their selective effects on P_{fusion} and P_{occ}, respectively.

Consistent with the effect of PDBU on Munc13-mediated docking/priming of vesicles and the lack of its effect on VGCC modulation, we detected no significant change in the peak amplitude of [Ca^{2+}] transients following its bath application (Figures 5D and 5G). During the same period, when 5 μM 4-AP was applied to the bath, a 46% ± 29% increase was detected (Figures 5E and 5G) in the peak amplitude of [Ca^{2+}] transients. The joint application of 4-AP and PDBU also caused a significant increase in the peak amplitude of [Ca^{2+}] transients, the magnitude of which was not significantly different from that observed when 4-AP was applied alone (Figures 5F–5H). In these experiments [Ca^{2+}] transients were pooled from all imaged boutons of the PCs (~16 boutons per cell) irrespective of their postsynaptic targets. When the drug effects were investigated in only those boutons that targeted PV- or mGluR1α-positive structures, similar significant increases were found for 4-AP and 4-AP + PDBU, but not for PDBU, for both synapse populations (Figure 5M).

Similar docked SV densities in AZs innervating FSINs and O-LM cells as revealed by high-resolution EM

Our paired-recording experiments with pharmacology indicate that P_{occ} contributes more than P_{fusion} to the low P_v at PC – O-LM cell synapses. The classical interpretation of low P_{occ} is that the RSs are not occupied by SVs in resting conditions. First, we examined this with EM on 20-nm-thick serial sections and reconstructed AZs innervating either FSIN (Figure 8A) or O-LM cell (Figure 8B) dendrites. These cells were intracellularly filled with biocytin in acute slices and were then fixed and processed for EM (see STAR Methods). Qualitatively, axon terminals innervating FSIN and O-LM dendrites looked very similar; they had similar size and many SVs were present along the AZ and also filled the majority of the boutons. The density of docked vesicles was not significantly different in the two AZ populations (FSIN: 115 ± 36 vesicle/μm^2, n = 15 AZs; O-LM: 121 ± 41 vesicle/μm^2, n = 21 AZs; Figure 8C). Although we cut extremely thin sections for our serial EM reconstructions, identifying whether an SV is in direct contact with the intracellular membrane leaflet of the plasma membrane might be less prone to error if one uses EM tomography. We therefore repeated these experiments on 200-nm-thick EM sections and obtained tilt image series for tomography. The visualizations of SVs and plasma membranes were indeed clearer in tomographic subvolumes (Figures 8D and 8E), allowing unequivocal determination of whether an SV is in direct contact with the plasma membrane or not. Despite this advantage of EM tomography, docked SV densities were also very similar in the AZs innervating FSINs (136 ± 35 SV/μm^2, n = 68 AZs in 3 mice) and O-LM cells (145 ± 41 SV/μm^2, n = 63 AZs in 3 mice; Figure 8F). We also compared the vesicle distributions within 100 nm of the AZs and found similar distribution profiles in the two synapse populations, and no difference could be detected in the spatial densities either (Figures 8G and 8H). Our EM data clearly demonstrate that RSs are similarly occupied by SVs at PC – FSIN and PC – O-LM cell synapses, but these SVs appear to be in different primed states at PC – FSIN compared to PC – O-LM IN synapses as depicted from our pharmacological experiments.

DISCUSSION

Using high-resolution immunolocalization of Munc13-1 and Cav2.1, here, we demonstrate that the nano-topology (both EZ models) and the distance (EZ radius: both ~40–50 nm) between VGCCs and the RSs are similar at PC – FSIN and PC – O-LM cell synapses, suggesting that the large difference in P_v is unlikely to be the consequence of a large difference in P_{fusion}. This is supported by the <2-fold difference in the effect of the K^+ channel blocker 4-AP on uEPSCs recorded from these two IN types. However, upon the application of the phorbol ester analog PDBU, a ~80% increase in the uEPSC amplitude of PC – FSIN connections is contrasted by a ~4.5-fold increase in the postsynaptic responses at PC – O-LM cell connections, suggesting that the docking/priming of the SVs is incomplete at AZs innervating O-LM cells. Our high-resolution EM analysis demonstrated that the docked SV density is similar at these two synapse populations, arguing against different P_{occ} between these synapses.

Our data show that most RSs are occupied by docked SVs, and, therefore, the P_{occ} is very high, consistent with the data of Sakamoto et al. (2018), showing an almost identical number of RSs and number of readily releasable SVs in cultured hippocampal neurons. It seems to be in odds with Malagon et al. (2020), but the data of Malagon et al. is consistent with a complete docking and incomplete priming of SVs. Our results are also consistent with those obtained from crayfish neuromuscular junctions where the low P_v tonic synapses have an even higher docked vesicle density than that found at the high-output phasic synapses, demonstrating that the P_v cannot be predicted from the number of docked vesicles (Millar et al., 2002). Furthermore, our results are in line with those of Millar et al. (2005), showing that when artificially imposing similar intra-bouton [Ca^{2+}] to tonic and phasic neuromuscular synapses, the outputs of the low P_v tonic synapses remain still lower despite the larger number of docked vesicles, indicating that most SVs in tonic synapses are molecular-release incompetent.

Since the discovery of the Ca^{2+}-dependence of neurotransmitter release (Del Castillo and Katz, 1954), one of the most

(B) Individual (thin traces) and their averaged (thick trace) uEPSCs evoked by three action potentials at 40 Hz are shown from the beginning (gray) and end (purple) of the recording period from the same pair (left). Superimposed averaged traces of the first uEPSCs at the beginning (black) and end (purple) of the recording (top, right). The amplitude of the first uEPSCs is unchanged at the beginning and end of a 30-min-long recording period without any drug application (bottom right; baseline: mean of 60 traces, 0–10 min; control (CTRL): mean of 60 traces, 20–30 min; p = 0.51, WSR test, n = 15 pairs in 15 mice).
(C–E) Same as (B), but either 5 μM 4-AP (red, C), the phorbol ester analog PDBU (1 μM, blue, D), or both (green, E) were applied to the slice after a 10-min baseline (black) recording period. All treatments significantly increased the amplitude of the first uEPSC (50% ± 59%, 77% ± 115% and 70% ± 61%, n = 12, 8, and 8 pairs; in 11, 8, and 8 mice, p = 0.025, 0.04, and 0.02 WSR test, respectively).
Horizontal lines in the boxplots: 25th, 50th, and 75th percentiles, rectangle: mean, whiskers: SD.

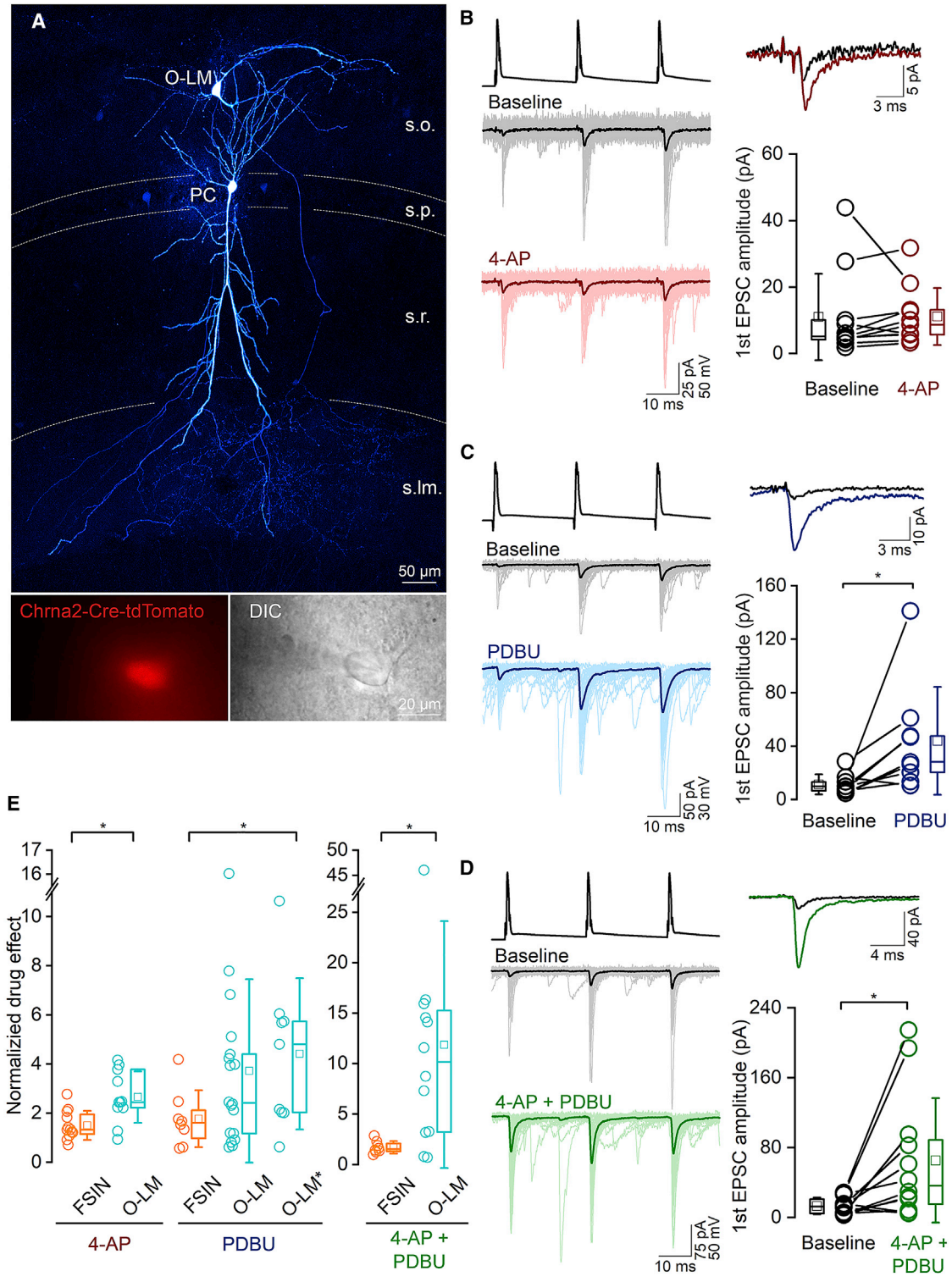

Figure 7. Robust PDBU sensitivity of uEPSCs in O-LM INs

(A) Confocal maximum intensity projection image of a biocytin-filled, synaptically connected PC – O-LM IN pair in the hippocampal CA1 region (top). Note the extensive axonal arbor of the O-LM IN in the stratum lacunosum moleculare (s.lm.). Bottom left: epifluorescent image of a tdTomato-positive IN, acquired prior to patching. Bottom right: DIC image of the same IN, with the patch pipette.

(B) Individual (thin traces) and the averaged (thick traces) uEPSCs evoked by three action potentials at 40 Hz are shown for the baseline (gray) and after 4-AP wash-in (red) of the recording period from the same pair (left). Superimposed averaged traces of the first uEPSCs at the beginning (black) and end (dark red)

(legend continued on next page)

obvious explanations of different presynaptic strengths is the distinct amount of Ca^{2+} entry into the presynaptic terminals upon an AP. Recent EM immunolocalization studies have established that presynaptic VGCCs are exclusively present in the AZs at central synapses (Bucurenciu et al., 2008; Holderith et al., 2012; Indriati et al., 2013; Kulik et al., 2004; Nakamura et al., 2015) where their numbers show large variability, suggesting indeed that the number of VGCCs should be a key determinant of the P_v. This notion was supported by the results of overexpression of Cav2.1 VGCC subunit in Calyx of Held, which induced an increase in P_v (Lubbert et al., 2019), and the results showing that the number of VGCCs and amount of Ca^{2+} influx correlate with P_v at individual RSs at Drosophila neuromuscular junction (NMJ; Akbergenova et al., 2018; Gratz et al., 2019; Newman et al., 2022). However, a recent study provided compelling evidence against such a simplistic view. The AZs of cerebellar parallel fibers to Purkinje cell synapses contain a high density of VGCCs and possess large AP-evoked [Ca^{2+}] transients, but the P_v is low, whereas cerebellar MLIN synapses have higher P_v despite having 5-fold lower VGCC numbers and small AP-evoked Ca^{2+} transients (Rebola et al., 2019). High-resolution localization of VGCCs and the RS marker Munc13-1 revealed distinct nano-topologies at these two synapses. A small number of VGCCs forms clusters close (10–20 nm) to the RSs in MLIN synapses, whereas, despite their large number (Nakamura et al., 2015; Rebola et al., 2019), VGCCs are excluded from a ~50 nm radius around the RSs in parallel fiber AZs. Thus, distinct nano-topologies and coupling distances of docked SVs and VGCCs at the AZs could overrule the simplistic view that more VGCCs and resulting higher Ca^{2+} influx make a synapse stronger and more reliable. Indeed, many other studies demonstrated distinct nano-topologies of RSs and VGCCs (e.g. rows of VGCCs are located along the SV [Dittrich et al., 2013; Luo et al., 2011; Neef et al., 2018], perimeter release model [Miki et al., 2017; Nakamura et al., 2015; Rebola et al., 2019], EZ model; [Keller et al., 2015; Rebola et al., 2019]), demonstrating that non-random, structured nano-topologies of RSs and VGCCs seem to be a general organizational principle, which is supported by our data at these two hippocampal glutamatergic synapses. However, our results at PC – FSIN and PC – O-LM cell synapses take this complexity to an even deeper level. Our SDS-FRL experiments showed similar nano-topologies and similar EZ radii at these functionally very different synapses, demonstrating the existence of molecular complexity with profound functional consequences beyond the nanoscale organization of VGCCs and RSs.

The similar nano-topologies and EZ radii at the PC – FSIN and PC – O-LM cell synapses, the moderate difference in the AP-evoked peak [Ca^{2+}] transients, and the effect of 4-AP point toward a small difference in the P_{fusion} at these synapses, which is clearly insufficient to explain the 10-fold differences in P_v. It seems logical to assume that the energy barrier for vesicle fusion for a given [Ca^{2+}] increase should be different at these synapses, implying distinct molecular mechanisms of vesicle tethering, docking, or priming. Because our high-resolution EM experiments demonstrated a similar density of docked vesicles at both synapse types, we can rule out dramatically different tethering and docking as a major difference, leaving molecular priming as the most likely scenario (Taschenberger et al., 2016; Wolfel et al., 2007). It is now generally accepted that Munc13 molecules are the master regulators of SV priming at central synapses (reviewed by Rizo, 2018). Our results, showing a dramatic difference in the effect of PDBU on EPSCs at PC – FSIN vs. PC – O-LM cell synapses, indicate that Munc13 molecules are the key players rendering different functions to these synapses, which can be achieved with different Munc13 isoforms or alternatively by differential regulation of the same isoform.

There are three centrally expressed Munc13 isoforms (Munc13-1 to 3; Brose et al., 1995), out of which CA1 PCs express Munc13-1 and Munc13-2 (Rosenmund et al., 2002). Munc13-1 has been associated with priming of vesicles with high efficiency, resulting in high P_v. In contrast, Munc13-2 (ubMunc13-2 and bMunc13-2) has been suggested to render synaptic vesicles low-P_v, resulting in postsynaptic responses that display short-term facilitation (Cooper et al., 2012; Man et al., 2015; Neher and Brose, 2018; Rosenmund et al., 2002). In a previous study (Holderith et al., 2022), we discovered that bMunc13-2 is selectively present in AZs of CA1 PCs that innervate som/mGluR1α-positive O-LM cells, making it a prime candidate to mediate the improper priming of SVs in this unreliable synapse. Despite its exquisite localization, conditional genetic deletion of Munc13-2 from CA1 PCs changed neither the peak amplitude nor the short-term plasticity of EPSCs at PC – O-LM cell connections, suggesting a minor, if any, effect of Munc13-2 in the priming process of vesicles at this low P_v synapse (Holderith et al., 2022). We have also shown that in these synapses Munc13-2 is not the only Munc13 isoform; they also contain Munc13-1 in a density that is higher than that found in the rest of the PC AZs. These data, taken together, demonstrate that SVs can be efficiently and inefficiently primed by Munc13-1

of the recording are on the top, right. The amplitude of the first uEPSCs is not significantly different at the beginning of the recording and after the application of 5 μM 4-AP (bottom right; baseline: mean of 60 traces, 0–10 min; 4-AP: mean of 60 traces, 20–30 min; p = 0.17, WSR test, n = 11 pairs in 9 mice). Presynaptic PCs were recorded in whole-cell configuration.

(C) Same as (B) but showing the effect of 1 μM PDBU on uEPSCs in O-LM cells. PDBU significantly increased the amplitude of first uEPSCs of the train (n = 9 pairs in 9 mice; p = 0.013 WSR test). Presynaptic PCs were recorded in perforated patch configuration.

(D) Same as (B) but demonstrating the effect of simultaneous application of PDBU and 4-AP (n = 12 pairs, in 11 mice, p = 0.009, WSR test). Presynaptic PCs were recorded in whole-cell configuration.

(E) Summary of the effects of different drugs on the amplitude of first uEPSCs recorded from O-LM cells and FSINs. Plots show normalized drug effects, corrected to the rundowns measured in control recordings for O-LM, but not for FSIN or for O-LM* (seeFigures 6B, S2A, and S2D). All data, apart from O-LM*, were obtained with presynaptic PCs recorded in the whole-cell configuration. Data indicated with O-LM* were obtained with PCs recorded in the perforated patch configuration. Statistical comparison between FS and O-LM was assessed with MWU test (p = 0.007 in 4AP, p = 0.16 in PDBU [FS vs. O-LM], p = 0.024 in PDBU [FS vs. O-LM*], p = 0.015 in 4-AP + PDBU).

Horizontal lines in the boxplots: 25th, 50th, and 75th percentiles, rectangle: mean, whiskers: SD.

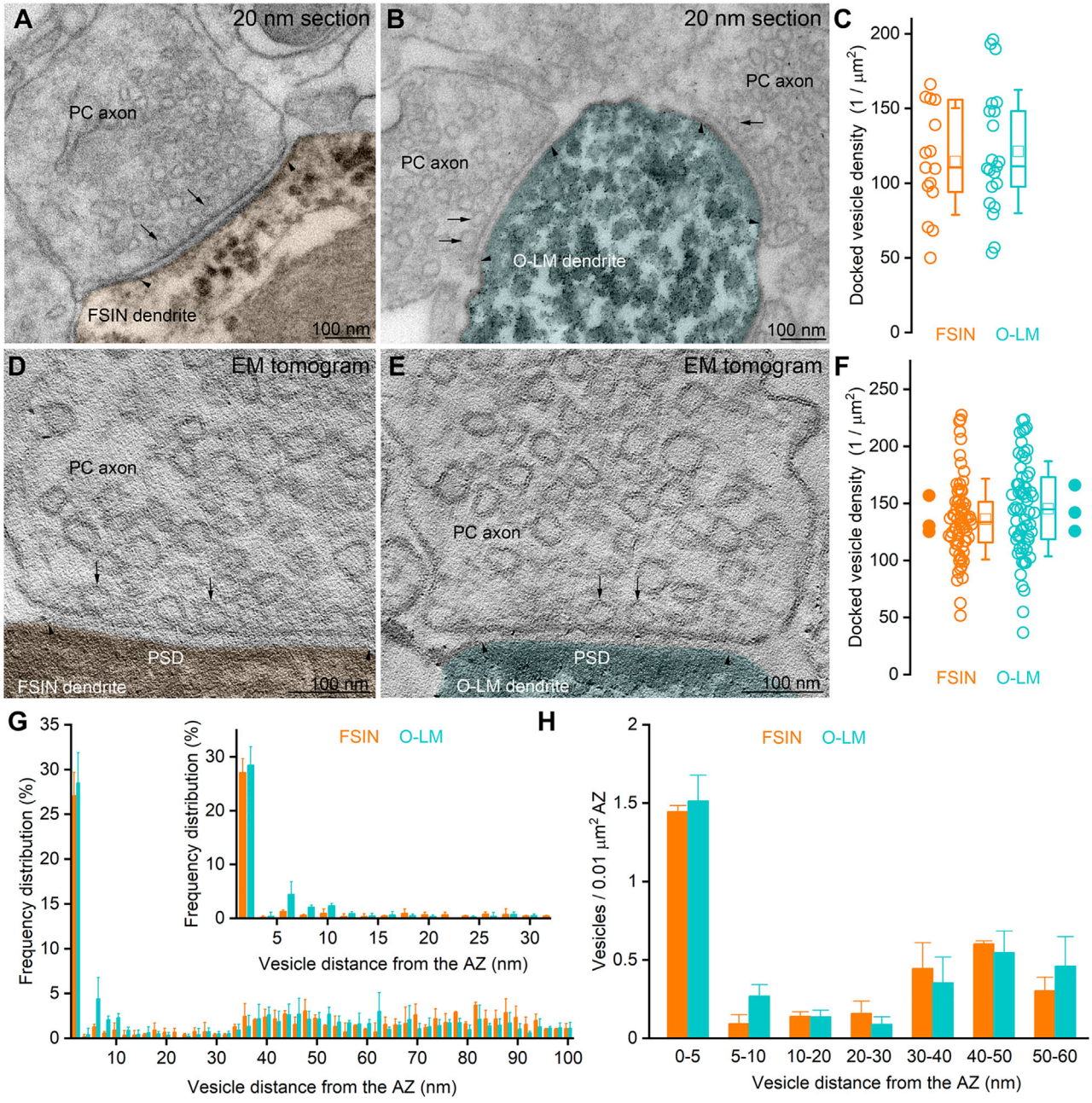

Figure 8. Serial section EM and EM tomography reveals similar densities of docked vesicles in AZs innervating O-LM and FSINs

(A and B) High magnification electron micrographs of 20-nm-thick sections showing excitatory synapses on an FSIN (A, orange) and an O-LM IN (B, cyan) dendrite. Arrowheads demarcate the edges of the synapses; arrows point to docked vesicles.

(C) Docked vesicles have similar densities in AZs reconstructed from serial 20-nm-thick sections that innervate FSIN and O-LM cell dendrites ($p = 0.9$, MWU test, $n = 15$ and 21 synapses in 1 mouse).

(D and E) Electron tomographic subvolumes (0.6 nm thick) of representative excitatory synapses on an FSIN (D, orange) and O-LM IN (E, cyan) dendrite. Arrowheads demarcate the edges of the synapses; arrows point to docked vesicles.

(F) Docked vesicles have similar densities in AZs innervating FSIN and O-LM cell dendrites ($p = 0.16$, MWU test, $n = 68$ FSIN and 63 O-LM cell targeting synapses in 4 mice). Densities were calculated from 200-nm-thick sections. Filled circles represent means within individual cells. Horizontal lines in the boxplots: 25th, 50th, and 75th percentiles, rectangle: mean, whiskers: SD.

(G) Spatial distribution of vesicles within 100 nm of the AZ membrane. Inset shows the spatial distribution within the first 30 nm ($n = 20$ FSIN and 30 O-LM cell targeting synapses in 3 mice). Data are shown as mean ± SD.

(H) Number (mean ± SD) of vesicles within bins of 5 and 10 nm distance from the AZ normalized to AZ area ($n = 20$ FSIN and 30 O-LM cell targeting synapses in 3 mice).

in hippocampal PC output synapses, depending on the postsynaptic partner.

Having excluded distinct Munc13 isoforms as the main reason for the functional differences, we must turn our focus to postsynaptic target cell-type-dependent differential regulations of Munc13-1. The C2A domain of Munc13-1 forms homodimers that prevent its docking and priming activity, which is liberated by the binding of Rab3-interacting molecule RIM (Camacho et al., 2017; Deng et al., 2011), making RIM a candidate for the differential regulation of Munc13-1. We tested this hypothesis in our previous study (Holderith et al., 2022) and found that the amounts of RIM1/2 in PC – O-LM synapses were similar to those found in the rest of the PC AZs, indicating that low P_v cannot be attributed to the unrelieved Munc13 autoinhibition by RIM in this low P_v synapse. Munc13-1 has been shown to form ~20-nm-long tethers, where the C1 and C2B domains form the plasma membrane anchors while the C2C domain attaches it to the vesicle membrane (Quade et al., 2019). In their non-activated form, C1-C2B domains prevent vesicle fusion via inhibiting the catalytic MUN domain that, together with Munc18, would orchestrate SNARE complex assembly through facilitating the opening of syntaxin (Li et al., 2019; Ma et al., 2011; Michelassi et al., 2017). Activity of C1 domain can be increased by the binding of diacylglyrecol (DAG) (produced by phospholipase C [PLC] upon increased intracellular [Ca^{2+}]) or phorbol esters like PDBU (Basu et al., 2007; Betz et al., 1998; Lou et al., 2005; Rhee et al., 2002). Indeed, a single point mutation in this domain that renders Munc13-1 constitutively active and phorbol ester insensitive results in increased SV release (Rhee et al., 2002). The priming activity of Munc13-1 can also be modulated by Ca^{2+} binding to the C2B domain, increasing its affinity to phosphatidylinositol phosphate (PIP) and PIP2 (Shin et al., 2010). Mutations that increased Ca^{2+}-dependent PIP2 binding enhanced neurotransmitter release. Although Ca^{2+} binding increases Munc13-1 binding to PIP- and PIP2-enriched membranes, the concentration of these molecules in the presynaptic plasma membrane is also an important factor: decreasing PIP or PIP2 concentration by 2-fold abolished Ca^{2+}-induced phospholipid binding of the C2B domain (Shin et al., 2010). These results, taken together, indicate that differential concentration of DAG and PIP/PIP2 in the presynaptic plasma membranes or the resting [Ca^{2+}] (Awatramani et al., 2005) might be responsible for the postsynaptic target cell-type-dependent distinct priming efficacy of Munc13-1.

How fast could an SV undergo molecular priming and become fusion competent? Hippocampal CA1 PC AZs that innervate FSIN have an average N of 5.5 and a P_v of 0.4, resulting in the release of ~2 out of the 3 release-ready SVs per AZ for the first AP, leaving only one release-ready SV at the AZ. If there was no replenishment/priming of SVs within 25 ms, only a single SV could be released by a second AP, resulting in a PPR of ~0.5. However, the PPR at 40 Hz at this synapse is 0.92, demonstrating that the second AP liberates 1.8 SVs. Thus, within 25 ms, either new SVs should diffuse to the RSs and get docked and primed, or, alternatively, the already docked but improperly primed SVs must undergo rapid molecular priming within this short time period. Understanding the dynamics of SV replenishment and priming during repeated presynaptic activity requires detailed experiments with short- and long-AP trains and fitting the data with a release model that accounts for different pools of vesicles with complex interactions between them (Eshra et al., 2021; Lin et al., 2022; Miki et al., 2016; Schneggenburger and Neher, 2000; Tran et al., 2022).

The most widely used method to examine the spatial distribution of SVs around AZs is serial section EM or EM tomography of aldehyde-fixed tissue. It has been proposed that aldehyde fixation can alter the number of docked and membrane-proximal SVs, thus calling into question the usefulness of this approach. High-pressure freezing followed by low-temperature embedding was then proposed as a method of choice to overcome the necessity of chemical fixation (Imig et al., 2014; Siksou et al., 2007). Although this method lacks potential chemical fixation artifacts, the examination of identified synapses of *in vivo* or *in vitro* recorded cells is almost impossible, presenting a major obstacle against using this as the sole method of choice. Although Maus et al. (2020) have demonstrated a sever loss of docked and membrane-proximal vesicles following perfusion fixation with a glutaraldehyde- and formaldehyde-containing fixative, they also provided evidence that immersion fixation with a glutaraldehyde- and formaldehyde-containing fixative resulted in docked vesicle densities that were very similar to those obtained following high-pressure freezing. Here, we applied the same immersion fixation procedure and found a significantly higher density of docked vesicles than in our previous study using perfusion fixation, although the species, the hippocampal subregion, and the age of the animals were also different (Eltes et al., 2017). The docked vesicle density values and distribution in this study (~140/μm^2) are very similar to those obtained in hippocampal cultures with high-pressure freezing, indicating that our method also preserves the distribution of vesicles in the presynaptic terminal (Imig et al., 2020; Maus et al., 2020). Here, we also measured the density of docked SVs at PC – O-LM synapses after high-pressure freezing and low-temperature dehydration (see STAR Methods) and found values (134 ± 50/μm^2, n = 3 mice) similar to those obtained following room-temperature dehydration (145 ± 41/μm^2, n = 3 mice). The similar density of docked SVs at the two types of AZs also highlights that the physical docking of SVs does not necessarily reflect molecular priming in an intact, genetically unperturbed synapse.

STAR★METHODS

Detailed methods are provided in the online version of this paper and include the following:

- KEY RESOURCES TABLE
- RESOURCE AVAILABILITY
  - Lead contact
  - Materials availability
  - Data and code availability
- EXPERIMENTAL MODEL AND SUBJECT DETAILS
  - Animals
- METHOD DETAILS
  - Slice preparation and electrophysiological recordings
  - Perforated patch-clamp recordings

- Two-photon laser scanning microscopy
- Tissue processing after two-photon imaging
- Tissue processing after paired whole-cell patch-clamp recordings
- Tissue processing for transmission EM and EM tomography
- High-pressure freezing of acute slices
- Freeze substitution
- EM tomography
- Immunofluorescent reactions
- Estimating the proportion of inhibitory synapses on mGluR1α+ INs
- SDS-digested freeze-fracture replica labeling

- QUANTIFICATION AND STATISTICAL ANALYSIS
  - Analysis of gold particle distributions labeling Munc13-1 and Cav2.1 within the AZs
  - Analysis of docked vesicle densities
  - Statistical analyses

SUPPLEMENTAL INFORMATION

Supplemental information can be found online at https://doi.org/10.1016/j.neuron.2022.09.035.

ACKNOWLEDGMENTS

Z.N. is the recipient of a European Research Council Advanced Grant (ERC-AG 787157) and a Hungarian National Brain Research Program (NAP2.0) grant. The financial support from these funding bodies is gratefully acknowledged. We thank Dóra Ronaszéki and Éva Dobai for their excellent technical assistance and Dr. Judit Makara for her advice in statistical analysis. The graphical abstract was created with Biorender (Biorender.com).

AUTHOR CONTRIBUTIONS

M.A., F.B., N.H., A.L., and Z.N. designed the experiments. M.A. and F.B. performed the *in vitro* paired recording and analyzed the data. N.H. performed the *in vitro* 2P imaging experiments and the EM work and analyzed her data. A.L. conducted SDS-FRL experiments and analyzed her data using the scripts written by M.R. Z.N. wrote the manuscript.

DECLARATION OF INTERESTS

The authors declare no competing interests.

INCLUSION AND DIVERSITY

We support inclusive, diverse, and equitable conduct of research.

Received: April 8, 2022
Revised: July 28, 2022
Accepted: September 27, 2022
Published: October 18, 2022

REFERENCES

Akbergenova, Y., Cunningham, K.L., Zhang, Y.V., Weiss, S., and Littleton, J.T. (2018). Characterization of developmental and molecular factors underlying release heterogeneity at Drosophila synapses. Elife *7*, e38268. https://doi.org/10.7554/eLife.38268.

Ali, A.B., Deuchars, J., Pawelzik, H., and Thomson, A.M. (1998). CA1 pyramidal to basket and bistratified cell EPSPs: dual intracellular recordings in rat hippocampal slices. The Journal of physiology *507* (Pt 1), 201–217. https://doi.org/10.1111/j.1469-7793.1998.201bu.x.

Ali, A.B., and Thomson, A.M. (1998). Facilitating pyramid to horizontal oriens-alveus interneurone inputs: dual intracellular recordings in slices of rat hippocampus. The Journal of physiology *507* (Pt 1), 185–199. https://doi.org/10.1111/j.1469-7793.1998.185bu.x.

Awatramani, G.B., Price, G.D., and Trussell, L.O. (2005). Modulation of transmitter release by presynaptic resting potential and background calcium levels. Neuron *48*, 109–121. https://doi.org/10.1016/j.neuron.2005.08.038.

Basu, J., Betz, A., Brose, N., and Rosenmund, C. (2007). Munc13-1 C1 domain activation lowers the energy barrier for synaptic vesicle fusion. J. Neurosci. *27*, 1200–1210. https://doi.org/10.1523/JNEUROSCI.4908-06.2007.

Betz, A., Ashery, U., Rickmann, M., Augustin, I., Neher, E., Sudhof, T.C., Rettig, J., and Brose, N. (1998). Munc13-1 is a presynaptic phorbol ester receptor that enhances neurotransmitter release. Neuron *21*, 123–136. https://doi.org/10.1016/s0896-6273(00)80520-6.

Biro, A.A., Holderith, N.B., and Nusser, Z. (2005). Quantal size is independent of the release probability at hippocampal excitatory synapses. J. Neurosci. *25*, 223–232. https://doi.org/10.1523/JNEUROSCI.3688-04.2005.

Brose, N., Hofmann, K., Hata, Y., and Sudhof, T.C. (1995). Mammalian homologues of Caenorhabditis elegans unc-13 gene define novel family of C2-domain proteins. J. Biol. Chem. *270*, 25273–25280. https://doi.org/10.1074/jbc.270.42.25273.

Bucurenciu, I., Kulik, A., Schwaller, B., Frotscher, M., and Jonas, P. (2008). Nanodomain coupling between Ca2+ channels and Ca2+ sensors promotes fast and efficient transmitter release at a cortical GABAergic synapse. Neuron *57*, 536–545. https://doi.org/10.1016/j.neuron.2007.12.026.

Camacho, M., Basu, J., Trimbuch, T., Chang, S., Pulido-Lozano, C., Chang, S.S., Duluvova, I., Abo-Rady, M., Rizo, J., and Rosenmund, C. (2017). Heterodimerization of Munc13 C2A domain with RIM regulates synaptic vesicle docking and priming. Nat. Commun. *8*, 15293. https://doi.org/10.1038/ncomms15293.

Cooper, B., Hemmerlein, M., Ammermuller, J., Imig, C., Reim, K., Lipstein, N., Kalla, S., Kawabe, H., Brose, N., Brandstatter, J.H., and Varoqueaux, F. (2012). Munc13-independent vesicle priming at mouse photoreceptor ribbon synapses. J. Neurosci. *32*, 8040–8052. https://doi.org/10.1523/JNEUROSCI.4240-11.2012.

Del Castillo, J., and Katz, B. (1954). Quantal components of the end-plate potential. The Journal of physiology *124*, 560–573. https://doi.org/10.1113/jphysiol.1954.sp005129.

Deng, L., Kaeser, P.S., Xu, W., and Sudhof, T.C. (2011). RIM proteins activate vesicle priming by reversing autoinhibitory homodimerization of Munc13. Neuron *69*, 317–331. https://doi.org/10.1016/j.neuron.2011.01.005.

Dittrich, M., Pattillo, J., King, J., Cho, S., Stiles, J., and Meriney, S. (2013). An excess-calcium-binding-site model predicts neurotransmitter release at the neuromuscular junction. Biophys. J. *104*, 2751–2763. https://doi.org/10.1016/j.bpj.2013.05.023.

Eltes, T., Kirizs, T., Nusser, Z., and Holderith, N. (2017). Target Cell Type-Dependent Differences in Ca(2+) Channel Function Underlie Distinct Release Probabilities at Hippocampal Glutamatergic Terminals. J. Neurosci. *37*, 1910–1924. https://doi.org/10.1523/JNEUROSCI.2024-16.2017.

Eshra, A., Schmidt, H., Eilers, J., and Hallermann, S. (2021). Calcium dependence of neurotransmitter release at a high fidelity synapse. Elife *10*, e70408. https://doi.org/10.7554/eLife.70408.

Ester, M., Kriegel, H.-P., Sander, J., and Xu, X. (1996). A density-based algorithm for discovering clusters in large spatial databases with noise. KDD-96 Proceedings, 226–231.

Gratz, S.J., Goel, P., Bruckner, J.J., Hernandez, R.X., Khateeb, K., Macleod, G.T., Dickman, D., and O'Connor-Giles, K.M. (2019). Endogenous Tagging Reveals Differential Regulation of Ca^{2+} Channels at Single Active Zones during Presynaptic Homeostatic Potentiation and Depression. J. Neurosci. *39*, 2416–2429. https://doi.org/10.1523/JNEUROSCI.3068-18.2019.

Gulyas, A.I., Megias, M., Emri, Z., and Freund, T.F. (1999). Total number and ratio of excitatory and inhibitory synapses converging onto single interneurons

of different types in the CA1 area of the rat hippocampus. J. Neurosci. *19*, 10082–10097. https://doi.org/10.1523/jneurosci.19-22-10082.1999.

Hagiwara, A., Fukazawa, Y., Deguchi-Tawarada, M., Ohtsuka, T., and Shigemoto, R. (2005). Differential distribution of release-related proteins in the hippocampal CA3 area as revealed by freeze-fracture replica labeling. The Journal of comparative neurology *489*, 195–216. https://doi.org/10.1002/cne.20633.

Holderith, N., Aldahabi, M., and Nusser, Z. (2021). Selective Enrichment of Munc13-2 in Presynaptic Active Zones of Hippocampal Pyramidal Cells That Innervate mGluR1α Expressing Interneurons. Front. Synaptic Neurosci. *13*, 773209. https://doi.org/10.3389/fnsyn.2021.773209.

Holderith, N., Lorincz, A., Katona, G., Rozsa, B., Kulik, A., Watanabe, M., and Nusser, Z. (2012). Release probability of hippocampal glutamatergic terminals scales with the size of the active zone. Nat. Neurosci. *15*, 988–997. https://doi.org/10.1038/nn.3137.

Imig, C., Lopez-Murcia, F.J., Maus, L., Garcia-Plaza, I.H., Mortensen, L.S., Schwark, M., Schwarze, V., Angibaud, J., Nagerl, U.V., Taschenberger, H., et al. (2020). Ultrastructural Imaging of Activity-Dependent Synaptic Membrane-Trafficking Events in Cultured Brain Slices. Neuron *108*, 843–860.e8. e848. https://doi.org/10.1016/j.neuron.2020.09.004.

Imig, C., Min, S.W., Krinner, S., Arancillo, M., Rosenmund, C., Südhof, T., Rhee, J., Brose, N., and Cooper, B. (2014). The morphological and molecular nature of synaptic vesicle priming at presynaptic active zones. Neuron *84*, 416–431. https://doi.org/10.1016/j.neuron.2014.10.009.

Indriati, D.W., Kamasawa, N., Matsui, K., Meredith, A.L., Watanabe, M., and Shigemoto, R. (2013). Quantitative localization of Cav2.1 (P/Q-type) voltage-dependent calcium channels in Purkinje cells: somatodendritic gradient and distinct somatic coclustering with calcium-activated potassium channels. J. Neurosci. *33*, 3668–3678. https://doi.org/10.1523/JNEUROSCI.2921-12.2013.

Karlocai, M.R., Heredi, J., Benedek, T., Holderith, N., Lorincz, A., and Nusser, Z. (2021). Variability in the Munc13-1 Content of Excitatory Release Sites. Elife *10*. https://doi.org/10.7554/eLife.67468.

Keller, D., Babai, N., Kochubey, O., Han, Y., Markram, H., Schurmann, F., and Schneggenburger, R. (2015). An Exclusion Zone for Ca2+ Channels around Docked Vesicles Explains Release Control by Multiple Channels at a CNS Synapse. PLoS Comput. Biol. *11*, e1004253. https://doi.org/10.1371/journal.pcbi.1004253.

Koester, H.J., and Johnston, D. (2005). Target cell-dependent normalization of transmitter release at neocortical synapses. Science, *308* (New York, NY), pp. 863–866. https://doi.org/10.1126/science.1100815.

Kremer, J.R., Mastronarde, D.N., and McIntosh, J. (1996). Computer visualization of three-dimensional image data using IMOD. J. Struct. Biol. *116*, 71–76. https://doi.org/10.1006/jsbi.1996.0013.

Kulik, A., Nakadate, K., Hagiwara, A., Fukazawa, Y., Lujan, R., Saito, H., Suzuki, N., Futatsugi, A., Mikoshiba, K., Frotscher, M., and Shigemoto, R. (2004). Immunocytochemical localization of the alpha1A subunit of the P/Q-type calcium channel in the rat cerebellum. Eur. J. Neurosci. *19*, 2169–2178. https://doi.org/10.1111/j.0953-816X.2004.03319.x.

Leao, R.N., Mikulovic, S., Leao, K.E., Munguba, H., Gezelius, H., Enjin, A., Patra, K., Eriksson, A., Loew, L.M., Tort, A.B.L., and Kullander, K. (2012). OLM interneurons differentially modulate CA3 and entorhinal inputs to hippocampal CA1 neurons. Nat. Neurosci. *15*, 1524–1530. https://doi.org/10.1038/nn.3235.

Lenkey, N., Kirizs, T., Holderith, N., Mate, Z., Szabo, G., Vizi, E.S., Hajos, N., and Nusser, Z. (2015). Tonic endocannabinoid-mediated modulation of GABA release is independent of the CB1 content of axon terminals. Nat. Commun. *6*, 6557. https://doi.org/10.1038/ncomms7557.

Li, L., Liu, H., Hall, Q., Wang, W., Yu, Y., Kaplan, J.M., and Hu, Z. (2019). A Hyperactive Form of unc-13 Enhances Ca(2+) Sensitivity and Synaptic Vesicle Release Probability in C. elegans. Cell Rep. *28*, 2979–2995.e4. e2974. https://doi.org/10.1016/j.celrep.2019.08.018.

Lin, K.H., Taschenberger, H., and Neher, E. (2022). A sequential two-step priming scheme reproduces diversity in synaptic strength and short-term plasticity. Proceedings of the National Academy of Sciences of the United States of America *119*. e2207987119. https://doi.org/10.1073/pnas.2207987119.

Lorincz, A., and Nusser, Z. (2010). Molecular identity of dendritic voltage-gated sodium channels. Science *328*, 906–909. https://doi.org/10.1126/science.1187958.

Losonczy, A., Somogyi, P., and Nusser, Z. (2003). Reduction of excitatory postsynaptic responses by persistently active metabotropic glutamate receptors in the hippocampus. Journal of neurophysiology *89*, 1910–1919. https://doi.org/10.1152/jn.00842.2002.

Lou, X., Scheuss, V., and Schneggenburger, R. (2005). Allosteric modulation of the presynaptic Ca2+ sensor for vesicle fusion. Nature *435*, 497–501. https://doi.org/10.1038/nature03568.

Lubbert, M., Goral, R.O., Keine, C., Thomas, C., Guerrero-Given, D., Putzke, T., Satterfield, R., Kamasawa, N., and Young, S.M., Jr. (2019). CaV2.1 α1 Subunit Expression Regulates Presynaptic CaV2.1 Abundance and Synaptic Strength at a Central Synapse. Neuron *101*, 260–273.e6. e266. https://doi.org/10.1016/j.neuron.2018.11.028.

Luo, F., Dittrich, M., Stiles, J.R., and Meriney, S.D. (2011). Single-pixel optical fluctuation analysis of calcium channel function in active zones of motor nerve terminals. J. Neurosci. *31*, 11268–11281. https://doi.org/10.1523/JNEUROSCI.1394-11.2011.

Ma, C., Li, W., Xu, Y., and Rizo, J. (2011). Munc13 mediates the transition from the closed syntaxin-Munc18 complex to the SNARE complex. Nat. Struct. Mol. Biol. *18*, 542–549. https://doi.org/10.1038/nsmb.2047.

Malagon, G., Miki, T., Tran, V., Gomez, L.C., and Marty, A. (2020). Incomplete vesicular docking limits synaptic strength under high release probability conditions. Elife *9*, e52137. https://doi.org/10.7554/eLife.52137.

Man, K.N.M., Imig, C., Walter, A.M., Pinheiro, P.S., Stevens, D.R., Rettig, J., Sorensen, J.B., Cooper, B.H., Brose, N., and Wojcik, S.M. (2015). Identification of a Munc13-sensitive step in chromaffin cell large dense-core vesicle exocytosis. Elife *4*, e10635. https://doi.org/10.7554/eLife.10635.

Maus, L., Lee, C., Altas, B., Sertel, S.M., Weyand, K., Rizzoli, S.O., Rhee, J., Brose, N., Imig, C., and Cooper, B.H. (2020). Ultrastructural Correlates of Presynaptic Functional Heterogeneity in Hippocampal Synapses. Cell Rep. *30*, 3632–3643.e8. e3638. https://doi.org/10.1016/j.celrep.2020.02.083.

Michelassi, F., Liu, H., Hu, Z., and Dittman, J.S. (2017). A C1-C2 Module in Munc13 Inhibits Calcium-Dependent Neurotransmitter Release. Neuron *95*, 577–590.e5. e575. https://doi.org/10.1016/j.neuron.2017.07.015.

Miki, T., Kaufmann, W.A., Malagon, G., Gomez, L., Tabuchi, K., Watanabe, M., Shigemoto, R., and Marty, A. (2017). Numbers of presynaptic Ca(2+) channel clusters match those of functionally defined vesicular docking sites in single central synapses. Proceedings of the National Academy of Sciences of the United States of America *114*, E5246–E5255. https://doi.org/10.1073/pnas.1704470114.

Miki, T., Malagon, G., Pulido, C., Llano, I., Neher, E., and Marty, A. (2016). Actin- and Myosin-Dependent Vesicle Loading of Presynaptic Docking Sites Prior to Exocytosis. Neuron *91*, 808–823. https://doi.org/10.1016/j.neuron.2016.07.033.

Millar, A.G., Bradacs, H., Charlton, M.P., and Atwood, H.L. (2002). Inverse relationship between release probability and readily releasable vesicles in depressing and facilitating synapses. J. Neurosci. *22*, 9661–9667. https://doi.org/10.1523/jneurosci.22-22-09661.2002.

Millar, A.G., Zucker, R.S., Ellis-Davies, G.C., Charlton, M.P., and Atwood, H.L. (2005). Calcium sensitivity of neurotransmitter release differs at phasic and tonic synapses. J. Neurosci. *25*, 3113–3125. https://doi.org/10.1523/JNEUROSCI.4717-04.2005.

Nakamura, Y., Harada, H., Kamasawa, N., Matsui, K., Rothman, J., Shigemoto, R., Silver, R., DiGregorio, D., and Takahashi, T. (2015). Nanoscale distribution of presynaptic Ca(2+) channels and its impact on vesicular release during development. Neuron *85*, 145–158. https://doi.org/10.1016/j.neuron.2014.11.019.

Neef, J., Urban, N.T., Ohn, T.L., Frank, T., Jean, P., Hell, S.W., Willig, K.I., and Moser, T. (2018). Quantitative optical nanophysiology of Ca(2+) signaling at inner hair cell active zones. Nat. Commun. *9*, 290. https://doi.org/10.1038/s41467-017-02612-y.

Neher, E. (2017). Some Subtle Lessons from the Calyx of Held Synapse. Biophys. J. *112*, 215–223. https://doi.org/10.1016/j.bpj.2016.12.017.

Neher, E., and Brose, N. (2018). Dynamically Primed Synaptic Vesicle States: Key to Understand Synaptic Short-Term Plasticity. Neuron *100*, 1283–1291. https://doi.org/10.1016/j.neuron.2018.11.024.

Newman, Z.L., Bakshinskaya, D., Schultz, R., Kenny, S.J., Moon, S., Aghi, K., Stanley, C., Marnani, N., Li, R., Bleier, J., et al. (2022). Determinants of synapse diversity revealed by super-resolution quantal transmission and active zone imaging. Nat. Commun. *13*, 229. https://doi.org/10.1038/s41467-021-27815-2.

Pouille, F., and Scanziani, M. (2004). Routing of spike series by dynamic circuits in the hippocampus. Nature *429*, 717–723. https://doi.org/10.1038/nature02615.

Quade, B., Camacho, M., Zhao, X., Orlando, M., Trimbuch, T., Xu, J., Li, W., Nicastro, D., Rosenmund, C., and Rizo, J. (2019). Membrane bridging by Munc13-1 is crucial for neurotransmitter release. Elife *8*, e42806. https://doi.org/10.7554/eLife.42806.

Quastel, D.J. (1997). The binomial model in fluctuation analysis of quantal neurotransmitter release. Biophys. J. *72*, 728–753. https://doi.org/10.1016/s0006-3495(97)78709-5.

Rebola, N., Reva, M., Kirizs, T., Szoboszlay, M., Lorincz, A., Moneron, G., Nusser, Z., and DiGregorio, D.A. (2019). Distinct Nanoscale Calcium Channel and Synaptic Vesicle Topographies Contribute to the Diversity of Synaptic Function. Neuron *104*, 693–710.e9. e699. https://doi.org/10.1016/j.neuron.2019.08.014.

Reddy-Alla, S., Bohme, M.A., Reynolds, E., Beis, C., Grasskamp, A.T., Mampell, M.M., Maglione, M., Jusyte, M., Rey, U., Babikir, H., et al. (2017). Stable Positioning of Unc13 Restricts Synaptic Vesicle Fusion to Defined Release Sites to Promote Synchronous Neurotransmission. Neuron *95*, 1350–1364.e12. e1312. https://doi.org/10.1016/j.neuron.2017.08.016.

Reyes, A., Lujan, R., Rozov, A., Burnashev, N., Somogyi, P., and Sakmann, B. (1998). Target-cell-specific facilitation and depression in neocortical circuits. Nat. Neurosci. *1*, 279–285. https://doi.org/10.1038/1092.

Rhee, J.S., Betz, A., Pyott, S., Reim, K., Varoqueaux, F., Augustin, I., Hesse, D., Sudhof, T.C., Takahashi, M., Rosenmund, C., and Brose, N. (2002). β Phorbol Ester- and Diacylglycerol-Induced Augmentation of Transmitter Release Is Mediated by Munc13s and Not by PKCs. Cell *108*, 121–133. https://doi.org/10.1016/s0092-8674(01)00635-3.

Ripley, B.D. (1979). Tests of Randomness for Spatial Point Patterns. J. Roy. Stat. Soc. B *41*, 368–374. https://doi.org/10.1111/j.2517-6161.1979.tb01091.x.

Rizo, J. (2018). Mechanism of neurotransmitter release coming into focus. Protein Sci. *27*, 1364–1391. https://doi.org/10.1002/pro.3445.

Rosenmund, C., Sigler, A., Augustin, I., Reim, K., Brose, N., and Rhee, J.S. (2002). Differential control of vesicle priming and short-term plasticity by Munc13 isoforms. Neuron *33*, 411–424. https://doi.org/10.1016/s0896-6273(02)00568-8.

Rozov, A., Burnashev, N., Sakmann, B., and Neher, E. (2001). Transmitter release modulation by intracellular Ca2+ buffers in facilitating and depressing nerve terminals of pyramidal cells in layer 2/3 of the rat neocortex indicates a target cell-specific difference in presynaptic calcium dynamics. The Journal of physiology *531*, 807–826. https://doi.org/10.1111/j.1469-7793.2001.0807h.x.

Sakamoto, H., Ariyoshi, T., Kimpara, N., Sugao, K., Taiko, I., Takikawa, K., Asanuma, D., Namiki, S., and Hirose, K. (2018). Synaptic weight set by Munc13-1 supramolecular assemblies. Nat. Neurosci. *21*, 41–49. https://doi.org/10.1038/s41593-017-0041-9.

Scanziani, M., Gahwiler, B.H., and Charpak, S. (1998). Target cell-specific modulation of transmitter release at terminals from a single axon. Proceedings of the National Academy of Sciences of the United States of America *95*, 12004–12009. https://doi.org/10.1073/pnas.95.20.12004.

Schneggenburger, R., and Neher, E. (2000). Intracellular calcium dependence of transmitter release rates at a fast central synapse. Nature *406*, 889–893. https://doi.org/10.1038/35022702.

Shigemoto, R., Kulik, A., Roberts, J.D.B., Ohishi, H., Nusser, Z., Kaneko, T., and Somogyi, P. (1996). Target-cell-specific concentration of a metabotropic glutamate receptor in the presynaptic active zone. Nature *381*, 523–525. https://doi.org/10.1038/381523a0.

Shin, O.H., Lu, J., Rhee, J.S., Tomchick, D.R., Pang, Z.P., Wojcik, S.M., Camacho-Perez, M., Brose, N., Machius, M., Rizo, J., et al. (2010). Munc13 C2B domain is an activity-dependent Ca2+ regulator of synaptic exocytosis. Nat. Struct. Mol. Biol. *17*, 280–288. https://doi.org/10.1038/nsmb.1758.

Siksou, L., Rostaing, P., Lechaire, J.P., Boudier, T., Ohtsuka, T., Fejtova, A., Kao, H.T., Greengard, P., Gundelfinger, E.D., Triller, A., and Marty, S. (2007). Three-dimensional architecture of presynaptic terminal cytomatrix. J. Neurosci. *27*, 6868–6877. https://doi.org/10.1523/JNEUROSCI.1773-07.2007.

Stachniak, T.J., Sylwestrak, E.L., Scheiffele, P., Hall, B.J., and Ghosh, A. (2019). Elfn1-Induced Constitutive Activation of mGluR7 Determines Frequency-Dependent Recruitment of Somatostatin Interneurons. J. Neurosci. *39*, 4461–4474. https://doi.org/10.1523/JNEUROSCI.2276-18.2019.

Sun, H.Y., Lyons, S.A., and Dobrunz, L.E. (2005). Mechanisms of target-cell specific short-term plasticity at Schaffer collateral synapses onto interneurones versus pyramidal cells in juvenile rats. The Journal of physiology *568*, 815–840. https://doi.org/10.1113/jphysiol.2005.093948.

Sylwestrak, E.L., and Ghosh, A. (2012). Elfn1 regulates target-specific release probability at CA1-interneuron synapses. Science, *338* (New York, NY), pp. 536–540. https://doi.org/10.1126/science.1222482.

Szoboszlay, M., Kirizs, T., and Nusser, Z. (2017). Objective quantification of nanoscale protein distributions. Sci. Rep. *7*, 15240. https://doi.org/10.1038/s41598-017-15695-w.

Taschenberger, H., Woehler, A., and Neher, E. (2016). Superpriming of synaptic vesicles as a common basis for intersynapse variability and modulation of synaptic strength. Proceedings of the National Academy of Sciences of the United States of America *113*, E4548–E4557. https://doi.org/10.1073/pnas.1606383113.

Tomioka, N.H., Yasuda, H., Miyamoto, H., Hatayama, M., Morimura, N., Matsumoto, Y., Suzuki, T., Odagawa, M., Odaka, Y.S., Iwayama, Y., et al. (2014). Elfn1 recruits presynaptic mGluR7 in trans and its loss results in seizures. Nat. Commun. *5*, 4501. https://doi.org/10.1038/ncomms5501.

Tran, V., Miki, T., and Marty, A. (2022). Three small vesicular pools in sequence govern synaptic response dynamics during action potential trains. Proceedings of the National Academy of Sciences of the United States of America *119*. e2114469119. https://doi.org/10.1073/pnas.2114469119.

Wolfel, M., Lou, X., and Schneggenburger, R. (2007). A mechanism intrinsic to the vesicle fusion machinery determines fast and slow transmitter release at a large CNS synapse. J. Neurosci. *27*, 3198–3210. https://doi.org/10.1523/JNEUROSCI.4471-06.2007.

STAR★METHODS

KEY RESOURCES TABLE

REAGENT or RESOURCE	SOURCE	IDENTIFIER
Antibodies		
Rabbit polyclonal anti-Munc13-1	Synaptic Systems	Cat# 126-103; RRID: AB_887733
Rabbit polyclonal anti-Kv3.1b	Synaptic Systems	Cat# 242 003; RRID: AB_11043175
Guinea pig polyclonal anti-Cav2.1	Synaptic Systems	Cat# 152 205; RRID: AB_2619842
Guinea pig polyclonal anti-mGluR1α	Synaptic Systems	Cat# mGluR1a-GP-Af660; RRID: AB_2571801
Rabbit polyclonal anti-Elfn1	Synaptic Systems	Cat# 448 003; RRID: AB_ 2884915
Guinea pig polyclonal anti-pan-AMPAR	Nittobo Medical	Cat# panAMPAR-GP-Af580; RRID: AB_2571610
Guinea pig polyclonal anti-$GABA_AR$ γ2	Synaptic Systems	Cat# 224 004; RRID: AB_10,594,245
Goat polyclonal anti-mGluR1a	Nittobo Medical	Cat# mGluR1a-Go-Af1220; RRID: AB_2571800
Mouse monoclonal ant-gephyrin	Synaptic Systems	Cat# 147 021; RRID: AB_2232546
Goat anti-rabbit IgG, 5nm gold	British Biocell International	Cat# EM.GAR5; RRID:AB_1769140
Goat anti-rabbit IgG, 10nm gold	British Biocell International	Cat# EM.GAR10; RRID:AB_2715527
Goat anti- guinea pig IgG, 15nm gold	British Biocell International	Cat# EM.GAG15;
Donkey anti-guinea pig IgG, 12nm gold	Jackson ImmunoResearch	Cat# 706-205-148; RRID:AB_2340465
Donkey anti-rabbit IgG, Alexa 488	Jackson ImmunoResearch	Cat# 711-545-152; RRID:AB_2313584
Goat anti-mouse IgG, Fc_Subclass 1 specific, Alexa 488	Jackson ImmunoResearch	Cat# 115-545-205; RRID:AB_2338854
Donkey anti-goat IgG, Cy3	Jackson ImmunoResearch	Cat# 705-165-147; RRID:AB_2307351
Donkey anti-guinea pig IgG, Cy3	Jackson ImmunoResearch	Cat# 706-165-148; RRID:AB_2340460
Donkey anti-guinea pig IgG, Alexa 647	Jackson ImmunoResearch	Cat# 706-605-148; RRID:AB_2340476
Donkey anti-rabbit IgG, Alexa 647	Jackson ImmunoResearch	Cat# 711-605-152; RRID:AB_2492288
Goat anti-guinea pig IgG, Abberior Star 580	Abberior	Cat# ST580-1006-500UG;
Goat anti-rabbit IgG, Abberior Star 635P	Abberior	Cat# ST635P-1002-500UG; RRID:AB_2893229
Streptavidin, Cy3 coupled	Jackson ImmunoResearch	Cat# 016-160-084; RRID:AB_2337244
Chemicals, peptides, and recombinant proteins		
Ketamine	Produlab Pharma B.V.	Cat# 2302/2/07
Xylazine	Produlab Pharma B.V.	Cat# 2303/3/07
Pipolphene	EGIS Gyógyszergyár Zrt.	Cat# OGYI-T-3086/01
K-gluconate	Sigma-Aldrich	Cat# P1847
Biocytin	Sigma-Aldrich	Cat# B4261
Alexa Fluor 594	Invitrogen	Cat# A10438
Fluo5F	Invitrogen	Cat# F14221
Phorbol 12,13-di-butyrate	Tocris	Cat# 4153
Paraformaldehyde	Molar Chemicals	Cat# BC0487491
Paraformaldehyde	EMS	Cat# 19208
Uranyle Acetate	TAAB	Cat# U008
Osmium tetroxide aqeous solution	Electron Microscopy Sciences	Cat# 19190
Osmium tetroxide crystal	Electron Microscopy Sciences	Cat# 19130
Durcupane ACM Resin Single component A	Sigma-Aldrich	Cat# 44611
Durcupane ACM Resin Single component B	Sigma-Aldrich	Cat# 44612
Durcupane ACM Resin Single component C	Sigma-Aldrich	Cat# 44613
Durcupane ACM Resin Single component D	Sigma-Aldrich	Cat# 44614
Picric acid	Sigma-Aldrich	Cat# 197378
Slowfade Diamond	Invitrogen	Cat# S36967

(*Continued on next page*)

Continued

REAGENT or RESOURCE	SOURCE	IDENTIFIER
Vectashield	Vector Laboratories	Cat# H-1000
Normal goat serum (NGS)	Vector Laboratories	Cat# S-1000
1-Hexadecene	Sigma-Aldrich	Cat# H700-9
Protein A-conjugated 10 nm gold	Cytodiagnostic	Cat# AC-10-05
Tannic acid	Sigma-Aldrich	Cat# T-0125
Gramicidin from *Bacillus aneurinolyticus* (*Bacillus brevis*)	Sigma-Aldrich	Cat# G5002
Experimental models: Organisms/strains		
Mouse C57Bl6/J	Jackson	Cat# JAX:000,664; RRID:IMSR_JAX:000,664
Mouse Tg(Chrna2-Cre)OE25Gsat/Mmucd	MMRRC	RRID:MMRRC_036502-UCD
Mouse Ai9 (Gt(ROSA)26Sor_CAG/LSL_tdTomato)	Jackson	Cat# JAX:007,909; RRID:IMSR_JAX:007,909
Mouse Ai (Gt(ROSA)26Sor_CAG/LSL_tdTomato)	Jackson	Cat# JAX:007,914; RRID:IMSR_JAX:007,914
Software and algorithms		
ImageJ	National Institute of Health	https://imagej.nih.gov/ij; RRID: SCR_003070
Mes v4.6	Femtonics	https://femtonics.eu/
Adobe Photoshop CS3	Adobe	https://www.adobe.com/hu/products/photoshop.html
OriginPro 2020b (Academic)	OriginLab	https://www.originlab.com/
Multiclamp (version 2.2)	Axon Instruments/Molecular Devices	https://www.moleculardevices.com/
Clampex (version 10.7)	Axon Instruments/Molecular Devices	https://www.moleculardevices.com/
Imod	Mastronade Group, University of Colorado	https://bio3d.colorado.edu/imod
SerialEM Version3.8.9	Mastronade Group, University of Colorado	https://bio3d.colorado.edu/SerialEM
MATLAB	Mathworks	N/A
GoldExt	Nusser Lab	http://www.nusserlab.hu/
Point Pattern Analysis	Rebola et al. (2019)	https://github.com/SynDiversity
Other		
Vibratome VT1200S	Leica	https://www.leica-microsystems.com/
Ultramicrotome EM UCT	Leica	https://www.leica-microsystems.com/
Olympus FV3000 Confocal microscope	Olympus	https://www.olympus-lifescience.com/
Femto 2D microscope	Femtonics	https://femtonics.eu/
Mai Tai femtosecond pulsing laser	Spectra-Physics	https://www.spectra-physics.com/
Nikon Eclipse FN1 microscope	Nikon	https://www.nikon.com/
Multiclamp 700B amplifier	Axon Instruments/ Molecular Devices	https://www.moleculardevices.com/
DMZ Zeits Puller	Zeitz	https://www.zeitz-puller.com/
Borosilicate glass capillary	Sutter Instruments	Cat# BF150-86-10
Jeol JEM1011 Transmission electronmicroscope	Jeol	https://www.jeol.co.jp/
Tecnai G2 Spirit BioTWIN transmission EM	Fei Europe Nanoport (Thermofisher Scientific)	https://www.fei.com/
Xarosa CMOS camera	EMSIS GmbH	https://www.emsis.eu/
Leica EM ACE900 Freeze Fracture System	Leica Microsystems	https://www.leica-microsystems.com/
Leica HPM100 High-Pressure Freezing System	Leica Microsystems	https://www.leica-microsystems.com/
Aluminum specimen carriers (type A)	Leica Microsystems	Cat# 16770141
Aluminum specimen carriers (type B)	Leica Microsystems	Cat# 16770142

RESOURCE AVAILABILITY

Lead contact

Further information and requests for resources and reagents should be directed to and will be fulfilled by the lead contact, Zoltan Nusser (nusser@koki.hu).

Materials availability

This study did not generate new unique reagents.

Data and code availability

- Any raw data supporting the current study is available from the lead contact upon request.
- The paper does not report original code.
- Any additional information required to reanalyze the data reported in this paper is available from the lead contact upon request.

EXPERIMENTAL MODEL AND SUBJECT DETAILS

Animals

One hundred forty seven adult (P50 – 85) male and female transgenic mice were used (Chrna2-Cre)OE25Gsat/Mmucd, (RRID:MMRRC_036502-UCD, on C57BL/6J background (Leao et al., 2012) crossed with reporter line Ai9 or Ai14 (Gt(ROSA) 26Sor_CAG/LSL_tdTomato). Seven C57BL/6J male mice (P49–63) were used for SDS-FRL experiments and three C57BL/6J male mice (P32–39) were used for immunofluorescent experiments. The animals were housed in the vivarium of the Institute of Experimental Medicine in a normal 12 h/12 h light/dark cycle and had access to water and food *ad libitum*. All the experiments were carried out in accordance with the Hungarian Act of Animal Care and Experimentation 40/2013 (II.14) and with the ethical guidelines of the Institute of Experimental Medicine Protection of Research Subjects Committee.

METHOD DETAILS

Slice preparation and electrophysiological recordings

One hundred forty mice were stably anesthetized with a ketamine, xylazine, pypolphene cocktail (0.625, 6.25, 1.25 mg/mL respectively, 10 μL/g body weight) then decapitated, the brain was quickly removed and placed into an ice-cold cutting solution containing the following (in mM): sucrose, 205.2; KCl, 2.5; $NaHCO_3$, 26; $CaCl_2$, 0.5; $MgCl_2$, 5; NaH_2PO_4, 1.25; and glucose, 10, saturated with 95% O_2 and 5% CO_2. Three hundred or 250 μm thick coronal slices were then cut from the dorsal part of the hippocampus using a Vibratome (Leica VT1200S) and were incubated in a submerged-type holding chamber in ACSF containing the following (in mM): NaCl, 126; KCl, 2.5; $NaHCO_3$, 26; $CaCl_2$, 2; $MgCl_2$, 2; NaH_2PO_4, 1.25; and glucose, 10, saturated with 95% O_2 and 5% CO_2, pH = 7.2–7.4, at 36°C, and were then kept at 22–24°C. Recordings were performed in the same ACSF supplemented with 2 μM AM251 to block presynaptic CB1 receptors either at 29–30°C for 2-photon imaging or 32–33°C for paired recordings up to 6 h after slicing.

Cells were visualized using either a Femto2D microscope equipped with oblique illumination and a water-immersion objective lens (25X, numerical aperture (NA) = 1.05, Olympus) or with infrared differential interference contrast (DIC) imaging on a Nikon Eclipse FN1 microscope and on a Luigs&Neumann microscope with Nikon Eclipse FN1 DIC components with a 40× water immersion objective (NA = 0.8). CA1 PCs were identified from their position and morphology. O-LM INs were identified in the stratum oriens of the CA1 region by the tdTomato expression and somatic morphology. FSINs were identified using their position, morphology and their membrane voltage responses upon de- or hyperpolarizing current injections (600 ms, from −300 to 800 pA with 50 pA steps). Patch pipettes (resistance 4–6 MΩ) were pulled from thick-walled borosilicate glass capillaries with an inner filament. Intracellular solution contained the following (in mM): K-gluconate, 130; KCl, 5; $MgCl_2$, 2; EGTA, 0.05; creatine phosphate, 10; HEPES, 10; ATP, 2; GTP, 1; and biocytin, 7; 10 mM glutamate was included for presynaptic PCs only, pH = 7.3; 290–300 mOsm. For two-photon [Ca^{2+}] imaging EGTA was omitted and 25 μM Alexa Fluor 594 and 200 μM Fluo5F (Invitrogen) were also added to the intracellular solution. Paired whole-cell recordings were performed (in 105 mice) while the PCs were held in the current-clamp mode at −65 mV (with a maximum of ±100 pA DC current), and postsynaptic INs held at −65 mV in voltage-clamp mode (with a maximum of ±200 pA DC current) with access resistance bellow 20 MΩ with a dual-channel amplifier (MultiClamp 700B; Axon Instruments). Three to five action potentials were evoked in the PC at 40 Hz with 1.2–1.5 ms-long depolarizing current pulses (1.5–2.2 nA) with 9 s inter-traces intervals. Peak amplitude and full width at half-maximal amplitude of the APs were monitored and cells were rejected if any of these parameters changed >10% during baseline recording. Data were filtered at 3–4 kHz (Bessel filter), digitized on-line at 50 kHz, recorded, and analyzed using Clampfit 10.7 and Clampfit 11.0 (Molecular Devices). INs with an increased access resistance (>25%) during the recording were excluded.

Perforated patch-clamp recordings

Perforated patch-clamp recordings were carried out from the presynaptic PCs to avoid rundown. The intracellular solution was supplemented with 100 μg/mL Gramicidin (freshly dissolved in DMSO on the recording day and used only for 2 h when dissolved in the intracellular solution) and 12 μM Alexa Fluo594. Pipette resistance was 18–25 MΩ and the pipette tip was back-filled with Gramicidin-free intracellular solution then with Gramicidin-containing intracellular solution. The spontaneous membrane rupture was regularly checked and if fluorescence was detected in the soma of the PC, the recording was discarded (e.g. Figure S2C). An average of 10–20 min was needed to achieve an access resistance of <150 MΩ and to start the paired recording protocols.

Two-photon laser scanning microscopy

Experiments were performed with a Femto2D (Femtonics) laser scanning microscope equipped with a MaiTai femtosecond pulsing laser tuned to 810 nm. Electrophysiological data and image acquisition were controlled with a MATLAB based software (MES, Femtonics). For detailed methods of Ca^{2+}-imaging see (Eltes et al., 2017; Holderith et al., 2012). Briefly cells (in 35 mice) were filled for 90 min with a Ca^{2+}-insensitive (25 μM Alexa Fluor 594) and a Ca^{2+}-sensitive fluorophore (200 μM Fluo5F). Boutons were selected at 50–300 μm distances from the soma, imaged in line scan mode at 1 kHz, with a laser intensity of 2–6 mW at the back aperture of the objective lens. Each bouton (on average 16 ± 8 per cell) was scanned once for baseline measurement, and once after washing in the control or drug solution for 10 min. Fluorescence changes upon 5 APs at 40 Hz were recorded. Only the peak amplitude of the $[Ca^{2+}]$ transient obtained for the first AP was quantified during the recording as $G/R_{(t)}=(F_{green(t)}-F_{rest,\ green})/(F_{red}-I_{dark,\ red})$ where $F_{green(t)}$ represents the green fluorescence signal as a function of time, $F_{rest,\ green}$ is the green fluorescence before stimulation, and $I_{dark,\ red}$ is the dark current in the red channel. To normalize data across batches of dyes, G_{max}/R values were measured by imaging a sealed (tip melted and closed by heating) pipette filled with intracellular solution containing 10 mM $CaCl_2$ for each cell at the same position where the boutons were imaged. G/R measurements from boutons were divided by G_{max}/R, yielding the reported values of G/G_{max}. All recordings were carried out at 29–30°C.

Tissue processing after two-photon imaging

After recordings, the slices were fixed in a solution containing 4% paraformaldehyde (FA, Molar Chemicals), 0.2% picric acid in 0.1 M phosphate buffer (PB), pH 7.4, at 4°C for 12–36 h. Slices were washed in 0.1 M PB and blocked in normal goat serum (NGS, 10%) for 1 h made in Tris-buffered saline (TBS; pH 7.4), incubated in the following primary antibodies: rabbit anti-PV (1:1000, RRID:AB_2156474; Synaptic Systems), guinea pig anti-mGluR1α (1:1000, RRID: AB_2571801; Frontier Institute), diluted in TBS containing 2% NGS and 0.2% Triton X-100. After several washes, the following secondary antibodies were applied: Alexa Fluor488-conjugated goat anti-rabbit and Cy5-conjugated donkey anti-guinea pig IgGs (1:500) diluted in TBS containing 2% NGS and 0.2% Triton X-100. Biocytin was visualized with Cy3-conjugated streptavidin (Jackson Immunoresearch; 1:500). Sections were mounted in Vectashield (Vector Laboratories). Image stacks were acquired with an Olympus FV1000 confocal microscope with a 20X or a 60× (oil-immersion) objective. Contacts between PC boutons and IN dendrites were considered as putative synapses if they had no apparent gap between them in the focal plane.

Tissue processing after paired whole-cell patch-clamp recordings

After recordings, the slices were fixed in a solution containing 4% FA, 0.2% picric acid in 0.1 M PB, pH = 7.4, at 4°C for 12 h. Slices were embedded in agarose (2%) and re-sectioned at 120–150 μm thickness. Biocytin was visualized with Cy3-conjugated streptavidin (1:1000) diluted in TBS containing 0.2% Triton X-100. Sections were mounted in Vectashield. Image stacks were acquired with an Olympus FV1000 confocal microscope with a 20X or a 60× (oil-immersion) objectives. Recorded INs were classified based on the dendritic and axonal arbors.

Tissue processing for transmission EM and EM tomography

After recordings, the slices were incubated in 1 uM TTX-containing ACSF for 10 min then fixed in a solution containing 4% FA (Electron Microscopic Sciences), 1.25% glutaraldehyde 0.2% picric acid in 0.1 M PB, pH = 7.4, at 4°C for 12 h, then kept in the same solution lacking glutaraldehyde prior to processing. Slices were cryopotected in 10 and 20% sucrose solution in 0.1 M PB, then repeatedly freeze-thawed above liquid nitrogen and were embedded in agarose (2%) and re-sectioned at 120–150 μm. Sections were treated with 1% sodium borohydrate and 1% H_2O_2. Biocytin was visualized using an avidin–biotin–horseradish peroxidase complex (Vector Laboratories) followed by a reaction with 3′3-diaminobenzidine tetrahydrochloride as chromogen and 0.01% H_2O_2 as oxidant for 12 min. For standard EM and EM tomography sections were then treated with 1% OsO_4 for 20 min, stained in 1% uranyl acetate for 25 min, dehydrated in a graded series of ethanol and embedded in epoxy resin (Durcupan). Series of 20 nm thick sections containing biocytin filled dendrites of the recorded INs were cut with an ultramicrotome (Leica Ultracut). Images from serial sections were taken with a JEOL JEM-1011 EM (EM, JEOL Ltd) of excitatory synapses on the biocytin filled IN dendrites. Active zones were reconstructed in 3D from consecutive serial sections. A vesicle was considered docked, when no gap was visible between the presynaptic plasma membrane and the vesicle membrane.

High-pressure freezing of acute slices

High-pressure freezing of acute slices from 3 mice containing biocytin-filled O-LM cells was carried out as in (Maus et al., 2020). Briefly after the visualization of the biocytin filled cells, sections were transferred into non-penetrating 20% BSA cryoprotectant dissolved in 0.1 M PB. Blocks from the CA1 area containing the filled cells were dissected and loaded into aluminum specimen carriers (type A, Leica Cat# 16770141, outer diameter 3 mm, inner cavity 200 μm) with slice surface side facing up and filled with the cryoproptectant. The filled carriers were loaded into the middle plates of the high-pressure freezing sample holder. Another carrier (type B, Leica Cat# 16770142) coated with 1-hexadecene served as lid with its flat side. The sample holder was loaded into the high-pressure freezing device (Leica HPM 100). Cryofixed samples were stored in liquid nitrogen until further processing.

Freeze substitution

Freeze substitution was performed as described in (Imig et al., 2014; Maus et al., 2020). Briefly, samples were incubated in 0.1% tannic acid in anhydrous acetone for 4 days at −90°C and then fixed with 2% OsO_4 in anhydrous acetone for 104 h, then the temperature was ramped up 5°C/hour, kept at −20°C for 16 h, then ramped up to 4°C and kept for 6 h. Samples were washed in acetone several times then embedded into Durcupan and polymerized at 56°C for 2 days 200 nm thick sections containing the filled cells dendrites were cut for EM tomography. We found no significant difference in the docked vesicle density (134 ± 50 vesicle/μm^2, n = 30 AZs targeting 3 O-LM cells in 3 mice, p = 0.09, MWU test) compared to that found following room temperature dehydration.

EM tomography

The method is described in detail in (Eltes et al., 2017). Briefly, 200 nm thick sections were cut and protein A-conjugated 10 nm gold particles (Cytodiagnostic) were applied on both sides as fiducial markers. Dendritic segments of recorded cells (3 FS and 3 O-LM cells from 4 mice) were selected in the stratum oriens. Single-axis tilt series of perpendicularly oriented synapses were acquired using a Tecnai G2 Spirit BioTWIN transmission EM operating at 120 kV and equipped with a Xarosa CMOS camera (EMSIS GmbH). Tilt series were recorded between ±60° (with 2° increments) at a 300,00× magnification using SerialEM software (https://bio3d.colorado.edu). Synapses were identified on the presence of a rigid membrane apposition between the pre- and postsynaptic membranes. As the dark precipitate of DAB masks the PSD at many synapses, glutamatergic synapses were distinguished from GABAergic ones on the basis of the sphericity of the vesicles. Furthermore the proportion of GABAergic input onto FSINs is ∼6% (Gulyas et al., 1999), and onto O-LM cells is 11% (Figure S3) suggesting minimal potential contribution of the inhibitory synapses to our sample. Tomographic volumes were reconstructed using the IMOD package (Imig et al., 2014; Kremer et al., 1996) and exported with binning 10 at z axis as *Z*-stacks for analysis (35 images per subvolume, resulting a 5 nm virtual pixel size in the *Z* dimension after compensation for shrinkage under the electron beam. AZ area and vesicle distance from the presynaptic membrane were measured with Reconstruct software (https://synapseweb.clm.utexas.edu) or in ImageJ. A vesicle was classified as docked if the outer part of the lipid bilayer was in direct contact with the inner part of the AZ membrane bilayer. As postsynaptic densities cannot be unequivocally identified in our samples, the ellipticity of the vesicles was used to distinguish glutamatergic and GABAergic synapses. We established that in our samples of identified glutamatergic synapses (postsynaptic partner unlabeled PC spine), SVs are mainly spherical with an ellipticity index close to 1 (0.9 ± 0.1, CV = 0.07, n = 51), whereas at GABAergic synapses (identified by PC soma as postsynaptic partner) SVs can be characterized with more diverse ellipticity (0.8 ± 0.1, CV = 0.16, n = 57), where elongated SVs are intermingled with round ones. Furthermore, considering the small proportion of inhibitory synapses targeting PV and O-LM INs (6 and 11% respectively, Figure S3), we predict that a potential contamination of our dataset with inhibitory synapses would only include 2–3 synapses in our sample of >60 synapses, having only a small influence on our conclusion.

Immunofluorescent reactions

Three C57BL/6J (P32 – P39) male mice were deeply anesthetized and were transcardially perfused with ice-cold fixative containing 4% FA, 0.2% picric acid in 0.1 M PB, pH = 7.4 or 1% FA in 0.1 M Na-acetate buffer pH = 6, for 15 min. 80 μm thick coronal sections from the dorsal hippocampus were cut and washed in 0.1M PB. Sections were blocked in normal goat or donkey serum (NGS or NDS, 10%) made up in Tris-buffered saline (TBS, pH = 7.4), followed by incubations in primary antibodies diluted in TBS containing 2% NGS and 0.1% Triton X-100. The following primary antibodies were used: rabbit polyclonal anti-Elfn1 (1:500; Synaptic Systems, SySy, Cat#. 448 003, RRID: AB_ 2884915), guinea pig polyclonal anti-pan-AMPAR (1:500; Nittobo Medical, Cat#. panAMPAR-GP-Af580, RRID: AB_2571610), guinea pig polyclonal anti-$GABA_AR$ γ2 (1:500; Synaptic Systems, SySy, Cat#. 224 004, RRID: AB_10,594,245), a guinea pig polyclonal mGluR1α (1:500, SySy, Cat# mGluR1α-GP-Af660, RRID: AB_2571801), a goat polyclonal anti-mGluR1α (1:500; Nittobo, Cat#. mGluR1α-Go-Af1220, RRID: AB_2571800), and a mouse monoclonal anti-gephyrin (1:1000; Synaptic Systems, SySy, Cat#. 147 021, RRID: AB_2232546) antibody. Following several washes in TBS, the following secondary antibodies were used to visualize the immunoreactions: Alexa 488 conjugated donkey anti-rabbit (1:500; Jackson Immunoresearch) or goat anti-mouse IgG1 (1:500, Jackson Immunoresearch), Cy3 conjugated donkey anti-goat (1:500, Jackson Immunoresearch) or donkey anti-guinea pig (1:500, Jackson Immunoresearch), Alexa 647 conjugated donkey anti-guinea pig (1:250; Jackson Immunoresearch) or donkey anti-rabbit (1:250, Jackson Immunoresearch), Abberior Star 580 conjugated goat anti-guinea pig (1:250, Abberior) and Abberior Star 635P conjugated goat anti-rabbit (1:250, Abberior). Images were taken with a confocal laser scanning microscope (FV3000, Olympus) using a 20× (NA = 0.85) or a 60× (NA = 1.35) objective.

Estimating the proportion of inhibitory synapses on mGluR1α+ INs

We have determined the proportion of inhibitory synapses on mGluR1α+ INs using multiple immunofluorescent reactions (Figure S3). The postsynaptic densities of excitatory synapses were labeled with Elfn1, and inhibitory synapses were either labeled with $GABA_AR$ γ2 subunit or gephyrin on mGluR1α+ INs (Figure S3B and C). We found that 11.1 ± 1.2% of the synapses are inhibitory (n = 3 mice) on mGluR1α+ INs. Proportion of SERT+, VAChT+ and VGlut2+ axons on mGluR1α+ INs is negligible compared to the excitatory synapses (data not shown).

SDS-digested freeze-fracture replica labeling

Four C57BL/6J (P49 – P63) male mice were deeply anesthetized and were transcardially perfused with ice-cold fixative containing 2% FA, 0.2% picric acid in 0.1 M PB for 15 min. 80 μm thick coronal sections from the dorsal hippocampus were cut, cryoprotected in 30% glycerol, and pieces from the CA1 area were frozen with a high-pressure freezing machine (HPM100, Leica Microsystems) and fractured in a freeze-fracture machine (EM ACE900, Leica) as described in (Lorincz and Nusser, 2010). Tissue debris were digested from the replicas with gentle stirring in a TBS solution containing 2.5% SDS and 20% sucrose (pH = 8.3) at 80°C for 18 h. The replicas were then washed in TBS containing 0.05% BSA and blocked with 5% BSA in TBS for 1 h followed by an incubation in a solution of the following antibodies: rabbit polyclonal anti-Kv3.1b (1:1600; Synaptic Systems, SySy, Cat#. 242 003, RRID: AB_11043175), rabbit polyclonal anti-Munc13-1 (1:200, SySy, Cat# 126 103, RRID: AB_887733), a guinea pig polyclonal anti-Cav2.1 (1:3000, SySy, Cat# 152 205, RRID: AB_2619842) and a guinea pig polyclonal anti-mGluR1α antibody (1:200, SySy, Cat# mGluR1a-GP-Af660, RRID: AB_2571801). This was followed by an incubation in 5% BSA in TBS containing the following secondary antibodies: goat anti-rabbit IgGs (GAR) coupled to 5 nm or 10 nm gold particles (1:80 or 1:100; British Biocell International, BBI) or donkey anti-guinea pig IgGs coupled to 12 nm gold particles (1:25, Jackson ImmunoResearch), or goat anti-guinea pig IgGs coupled to 15 nm gold particles (1:100, BBI). Finally, replicas were rinsed in TBS and distilled water before they were picked up on parallel bar copper grids and examined with a JEOL JEM-1011 EM (JEOL Ltd)). The Munc13-1 and Cav2.1 antibodies were raised against intracellular epitopes, resulting in a labeling on the protoplasmic face (P-face), therefore nonspecific labeling was determined on surrounding exoplasmic-face (E-face) plasma membranes and was found to be 5.7 ± 0.8 and 0.8 ± 0.3 gold particle/μm^2, respectively. To study the spatial distribution of Munc13-1 and Cav2.1 in the AZs of axon terminals targeting either Kv3.1b or mGluR1α positive dendrites and somata, all experiments were performed using the "mirror replica method" (Eltes et al., 2017; Hagiwara et al., 2005). With this method, replicas are generated from both matching sides of the fractured tissue surface, allowing the examination of the corresponding E− and P-faces of the same membranes. The AZs were delineated on the P-face based on the underlying high density of intramembrane particles. In the hippocampal AZs, labeling specificity was previously confirmed with SDS-FRL for both the Munc13-1 (Karlocai et al., 2021) and the Cav2.1 (Holderith et al., 2012) antibodies.

QUANTIFICATION AND STATISTICAL ANALYSIS

Analysis of gold particle distributions labeling Munc13-1 and Cav2.1 within the AZs

To analyze gold particle distributions we used a Python-based software with a graphical user interface, GoldExt (Szoboszlay et al., 2017) available on the website: www.nusserlab.hu/software.html and a MATLAB-based Point-Pattern-Analysis code package (Rebola et al., 2019) (https://github.com/SynDiversity). Coordinates of the immunogold particles and corresponding AZ perimeters were obtained from EM images in GoldExt. Munc13-1 labeling of AZs on Kv3.1b + structures was also analyzed in (Karlocai et al., 2021). Excitatory AZs were outlined manually based on visual inspection of the loose cluster of IMPs formed on axonal PFs. Such loose clusters are typically not formed on PF membranes of inhibitory AZs (Lenkey et al., 2015; Rebola et al., 2019). Gold particles labeling Munc13-1 and Cav2.1 were concentrated over the loose cluster of IMPs in excitatory AZs, and they were rare in the extrasynaptic membrane areas. We included gold particles neighboring the periphery of the IMP clusters, due to the spatial constraints coming from the size of primary and secondary antibodies. To estimate the potential error in manual demarcation of AZs, we manually marked each IMP over axonal membrane areas including potential AZs and extrasynaptic membranes, then performed DBSCAN cluster analysis and compared the area of IMP clusters to our manually demarcated AZ areas (Figure S1). Manually outlined AZ areas largely overlapped (92 ± 4%, CV = 0.04, n = 10) with the AZ areas determined by DBSCAN clustering of IMPs (Figure S1E). The density of IMPs within the AZs (2203.6 ± 489 IMP/μm^2) was 2.5 ± 1 times larger than in the surrounding areas (948.9 ± 244 IMP/μm^2; Figure S1F), confirming our visual impression. For NND analysis, we calculated the mean of the NNDs of all gold particles labeling either Munc13-1 or Cav2.1 and that of random distributed gold particles within the same AZ (same number of gold particles, 200 repetitions). The mean NNDs were then compared statistically using KW test followed by WSR test (paired comparison between data and random distribution) and Mann-Whitney-test (comparison of experimental NNDs between the two AZ populations) with HBC. We used a variance normalized and boundary corrected version of the Ripley's K function, called H-function to examine whether particle distributions within individual AZs are clustered or dispersed over a range of spatial scales (Rebola et al., 2019; Ripley, 1979). To determine the number of clusters in Munc13-1 labeled AZs we used the density-based clustering algorithm, DBSCAN (Ester et al., 1996). DBSCAN requires two user-defined parameters: ε (nm), which is the maximum distance between two localization points to be assigned to the same cluster, and *MinPts*, the minimum number of points within a single cluster. We systematically changed the ε value from 1 to 100 nm and found the largest difference between the data and the random distributions at ε = 31 nm for AZs on Kv3.1b structures. We then used *MinPts* = 2 and ε = 31 nm in our DBSCAN analysis for both AZ populations.

Variance normalized and boundary corrected bivariate Ripley's H-function (H_{biv}) was used to analyze the spatial relationship between particles labeling Munc13-1 and Cav2.1 (Rebola et al., 2019; Ripley, 1979). Bivariate Ripley's H-function indicates if two point-patterns are independent, exhibit attraction (clustered) or repulsion (dispersed). The 99% confidence envelopes (CEs) for Hbiv function were calculated from random patterns, generated by reassigning randomly each original particle either as a Munc13-1 or $Ca_V2.1$ particle (50 simulations per AZ). To compare H_{biv} functions at population level, we pooled different Hbiv functions from the different patterns across independent AZs. We used the 99% CE estimated from the random pattern simulations to scale the individual Hbiv function for each AZ. Normalized H_{biv} functions of individual AZs were then compared to the normalized population mean of random patterns with MAD test. The non-random, but not clustered distribution of Cav2.1 in our study is similar to that in cerebellar parallel fiber AZs, where Cav2.1 particles were also shown to be excluded from a certain area around synaptic vesicles (EZ). In our EZ model (based on (Rebola et al., 2019; Ripley, 1979), we calculated the coordinates of Munc13-1 cluster centers for each AZ and considered them as the center of docked synaptic vesicles for the given AZ. Circular areas of a fixed radius (30, 40, 50, 55 and 60 nm) around the cluster centers were considered as EZ areas. To simulate Cav2.1 patterns, same number of points as the measured number of particles were randomly distributed within the area of the AZ except for the EZ areas (50 simulations per AZ). Mean NNDs were then calculated for the measured and simulated patterns and were compared (Friedman test followed by WSR test with HBC).

Analysis of docked vesicle densities

AZ area and vesicle distance from the presynaptic membrane were measured with Reconstruct software (https://synapseweb.clm.utexas.edu) or in ImageJ.

Statistical analyses

Data is presented as mean ± SD throughout the MS, and 'n' represents number of cells, recorded cell pairs, synapses as appropriate unless stated otherwise in the text. Shapiro-Wilk test was used to test the normality of our data. The following statistical tests were used unless otherwise stated: to compare two dependent groups paired t test or Wilcoxon signed-rank (WSR) test, to compare two independent groups either unpaired t test or MWU test was used. To compare multiple populations of data Kruskal-Wallis (KW) test was used followed by WSR test or MWU test with Holm-Bonferroni correction (HBC). Statistical tests were performed in OriginPro (2020) (OriginLab) statistical significance was assessed at $p < 0.05$.

Neuron, Volume *110*

Supplemental information

Different priming states of synaptic vesicles underlie distinct release probabilities at hippocampal excitatory synapses

Mohammad Aldahabi, Flora Balint, Noemi Holderith, Andrea Lorincz, Maria Reva, and Zoltan Nusser

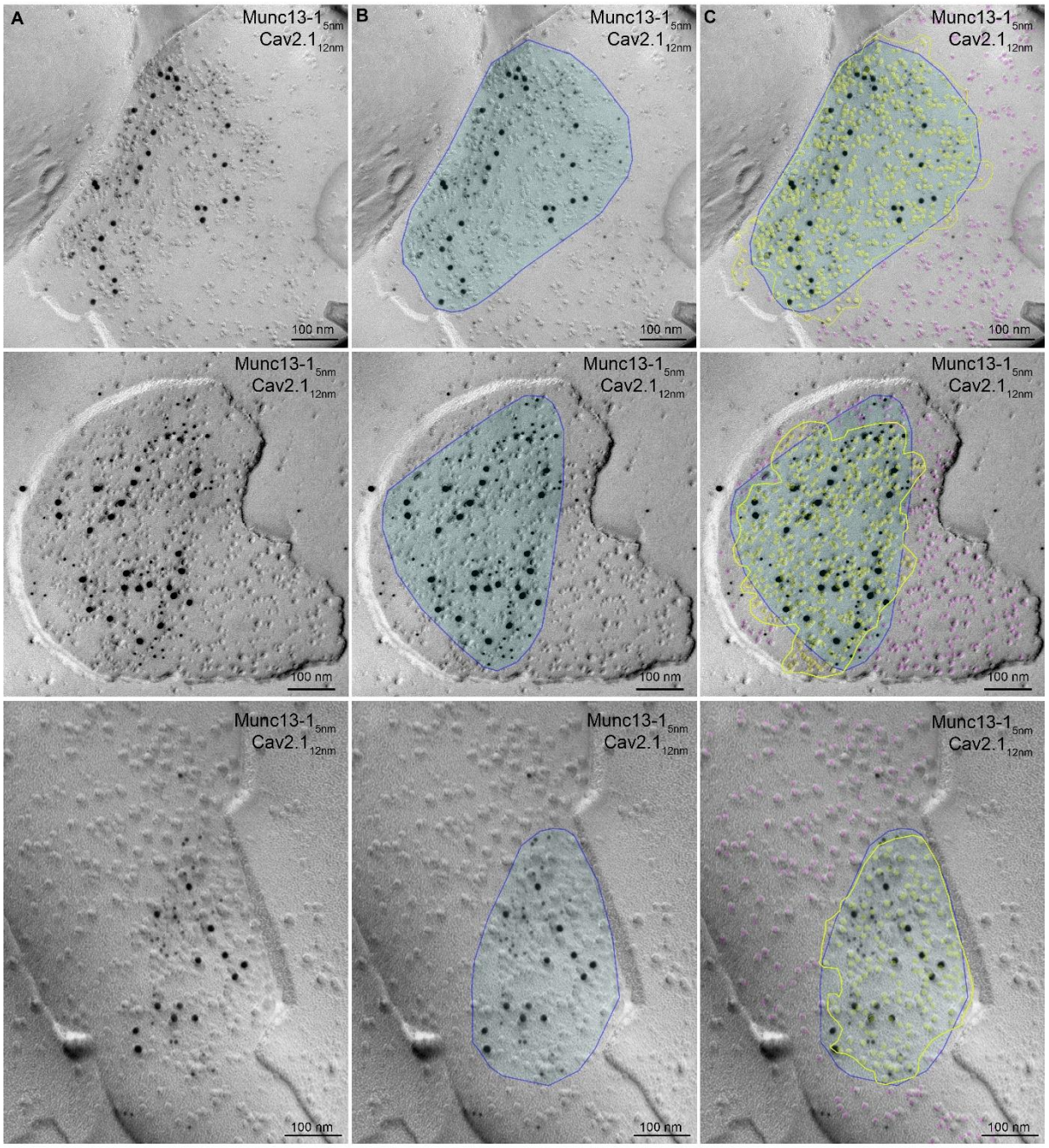
A
B
C
Munc13-1 5nm
Cav2.1 12nm
100 nm
D
AZ area (μm²)
0.4
0.3
0.2
0.1
0
Manual DBSCAN
E
Area overlap
(% of DBSCAN area)
100
75
50
25
0
F
IMP density (1/μm²)
3000
2500
2000
1500
1000
500
0
intra cluster
extra cluster

Figure S1: Comparison of active zone (AZ) areas determined by visual inspection or DBSCAN based outlining, Related to figure 2.

(A) Raw images of three axon terminal P-faces labeled for Munc13-1 and Cav2.1 with gold particles.

(B) AZ areas (blue) are outlined manually based on visual inspection of loose clusters of IMPs.

(C) AZ areas (yellow) are outlined based on DBSCAN clustering of all IMPs on the axonal P-face. Yellow dots label IMPs within the cluster, purple dots label IMPs outside the cluster.

(D) AZ areas determined by manual (blue) or DBSCAN based (yellow) outlining in 10 axon terminals.

(E) Manually outlined AZ areas largely overlap (mean ± SD = 92 ± 4%, CV = 0.04, n = 10) with the AZ areas determined by DBSCAN clustering of IMPs.

(F) Density of IMPs within DBSCAN determined clusters (2203.6 ± 489 IMP / μm^2) is on average 2.5 ± 1 times higher than outside the cluster (= 948.9 ± 244 IMP / μm^2).

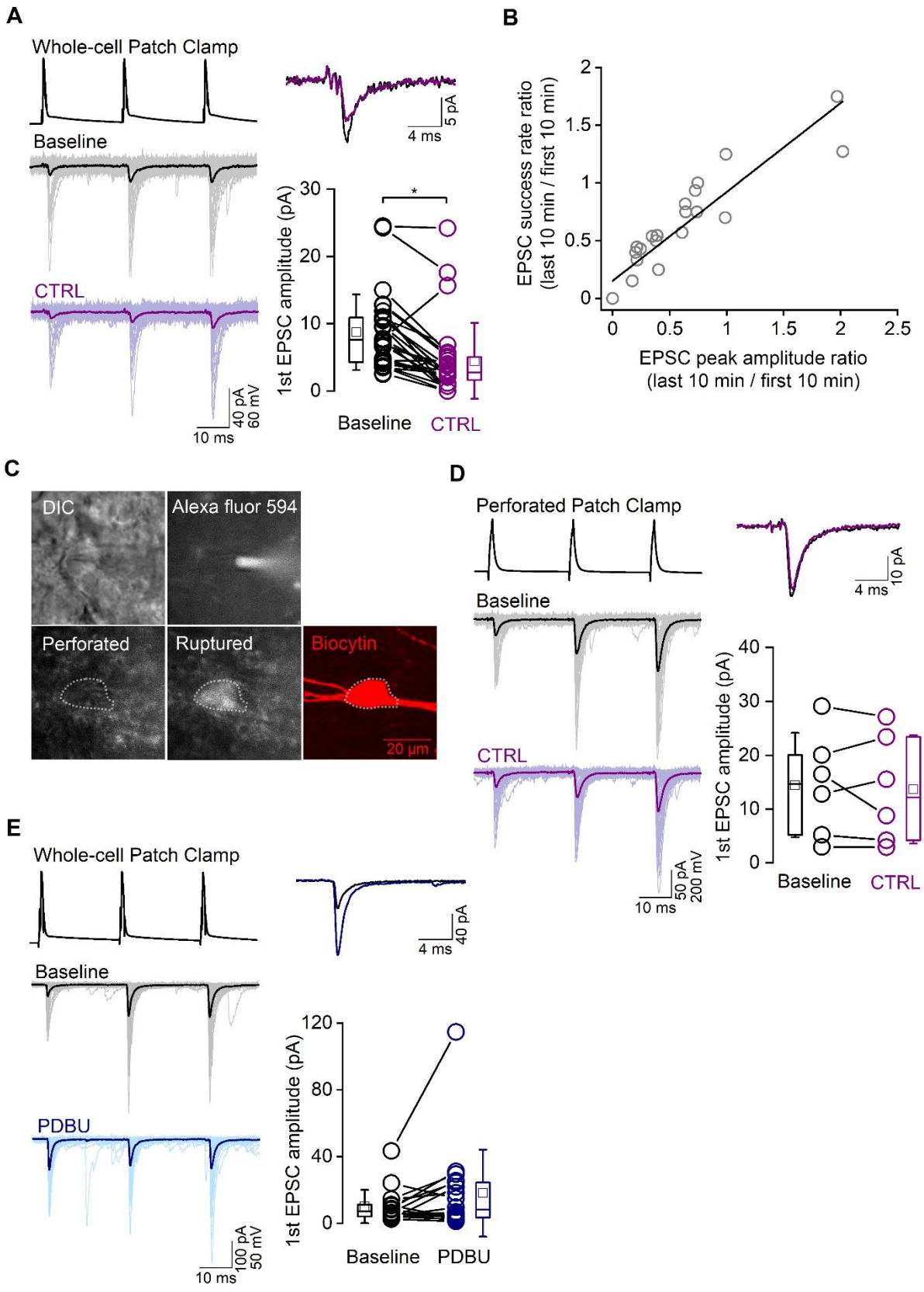
A
Whole-cell Patch Clamp
Baseline
CTRL
5 pA
4 ms
40 pA
60 mV
10 ms
1st EPSC amplitude (pA)
Baseline
CTRL
B
EPSC success rate ratio
(last 10 min / first 10 min)
EPSC peak amplitude ratio
(last 10 min / first 10 min)
C
DIC
Alexa fluor 594
Perforated
Ruptured
Biocytin
20 µm
D
Perforated Patch Clamp
Baseline
CTRL
10 pA
4 ms
50 pA
200 mV
10 ms
1st EPSC amplitude (pA)
Baseline
CTRL
E
Whole-cell Patch Clamp
Baseline
PDBU
40 pA
4 ms
100 pA
50 mV
10 ms
1st EPSC amplitude (pA)
Baseline
PDBU

Figure S2: Robust rundown of uEPSCs at CA1 PC – O-LM connections during 30 minutes of paired whole-cell recordings, Related to figure 7.

(A) Reduction of the amplitude of uEPSCs recorded in O-LM cells when the presynaptic PCs are recorded in whole-cell configuration. Individual (thin traces) and averaged (thick traces) uEPSCs evoked by three action potential at 40 Hz are shown from the beginning (black) and end (purple) of the recording period from the same pair (left). Superimposed averaged traces of the 1st uEPSCs at the beginning (black) and end (purple) of the recording (top right). The amplitude of the 1st uEPSCs is significantly reduced ($n = 28$, $p = 0.0001$, Wilcoxon signed-rank test) from the beginning (0 – 10 minutes) to the end (20 – 30 minutes) of a 30-minute-long recording period without any drug application (bottom right).

(B) Scatter plot between the uEPSCs peak amplitude ratios (last 10 min / first 10 min) and the success rate ratios (last 10 min / first 10 min) demonstrates that a larger rundown is accompanied by a larger increase in failure rate.

(C) Perforated patch-clamp recording of a PC. Differential interference contrast (DIC) image of a PC with an attached gramicidin-containing pipette after sealing (top, left). An epifluorescent image of the Alexa Fluor 594 filled pipette (top, right). After perforation of the membrane, the fluorophore in the pipette does not diffuse into the PC (bottom, left). When the plasma membrane ruptures, the Alexa 594 fluorophore diffuses into the PC (bottom, center). Maximum intensity projection image of the same PC after developing the biocytin with Cy3-coupled streptavidin.

(D) uEPSCs does not show a significant rundown ($n = 6$, $p = 0.83$, Wilcoxon signed-rank test) when the presynaptic PC is recorded in the perforated patch-clamp configuration. Panels are the same as in A.

(E) The effect of 1 μM PDBU on the uEPSCs when the presynaptic PCs were recorded in the whole-cell patch-clamp configuration. Panels are the same as in A. PDBU does not have a significant effect when not-corrected for the rundown ($n = 18$, $p = 0.117$, Wilcoxon signed-rank test). Box plots represent interquartile range, squares and whiskers indicate mean and SD in all panels.

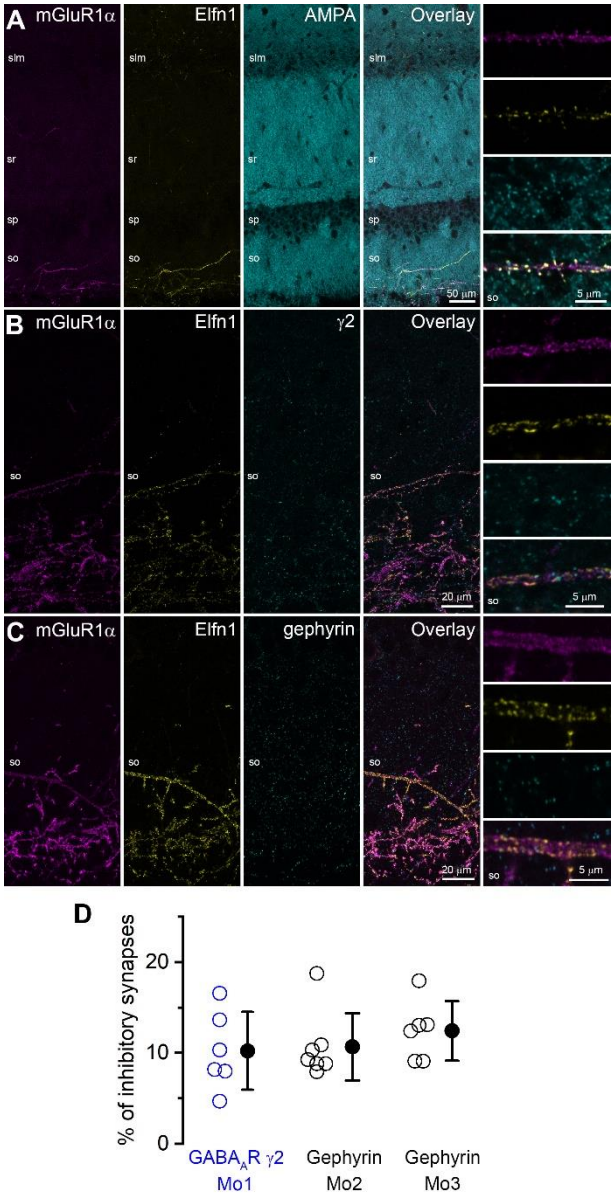

Figure S3: Distribution of inhibitory synapses on mGluR1α+ INs in CA1 stratum oriens, Related to STAR Methods.

(A) Immunofluorescent labeling for Elfn1, AMPA receptors and mGluR1α+ in the hippocampal CA1 area. (A right) High magnification view of a representative mGluR1α+ dendrite in stratum oriens (so) shows co-localization of Elfn1 and AMPA receptors.

(B) Immunofluorescent labeling for Elfn1, $GABA_AR$ γ2 subunit and mGluR1α+ in CA1 so. (B right) High magnification view of a representative mGluR1α+ dendrite.

(C) Immunofluorescent labeling for Elfn1, gephyrin and mGluR1α+ in CA1 so. (C right) High magnification view a representative mGluR1α+ dendrite.

(D) Percentage of inhibitory synapses on mGluR1α+ dendrites in so (n = 3 mice; Mo1, 10.2 ± 4.3%; Mo2, 10.7 ± 3.7%, Mo3, 12.4 ± 3.3 %). The proportion was calculated as the number of γ2 / gephyrin positive puncta divided by the sum of Elfn1 and γ2 /gephyrin puncta. Open circles indicate individual dendrites, filled circles represent mean ± SD.